First Large Capsule Implosions in a Frustum-shaped Hohlraum

K. L. Baker, P. A. Amendt, J. S. Ross, V. S. Smalyuk, O. L. Landen, D. D. Ho, S. Khan, J.D. Lindl, D. Mariscal, J. L. Milovich, S. MacLaren, Y. Ping, D. Strozzi, R. Bionta, D. Casey, P.M. Celliers, D. Fittinghoff, K. D. Hahn, M. Gatu Johnson, K. Meaney, M. Millot, R. Nora, C. Wilde

Abstract 40

We report on the first indirect-drive implosions driven by a dual conical frustum-shaped hohlraum denoted "frustraum" and the experimental tuning campaigns leading up to two layered implosions. The campaign utilized 1.2 mm and 1.4 mm inner radius HDC capsules and represented the largest HDC capsules to be imploded on the National Ignition Facility via indirect drive. Several techniques were successfully implemented to control the mode 2 symmetry of the implosions including changing the wall angle of the frustraum which is not possible with cylindrical hohlraums. A mode 4 feature was observed and its implications for hot spot mix discussed. Two layered implosions were conducted with 1.2 mm inner radius capsules, the latter of which achieved the highest layered capsule absorbed energy on the NIF using only 1.74 MJ of laser energy. The layered implosion results suggest that increasing capsule absorbed energy by itself is insufficient, and that further reducing coast time (time between end of laser pulse and bang time) to the 1 ns level is warranted to improve areal density, hot spot temperature and alpha heating and yield amplification.

I. INTRODUCTION

In indirect drive inertial confinement fusion (ICF) at NIF, a deuterium-tritium (DT) filled capsule[1, 2]is driven by the ablation pressure from x-rays at a peak radiation temperatures Tr of around 300 eV produced by irradiating the inside of a high-Z hohlraum with 192 laser beams entering through two laser entrance holes (LEHs) on either end. The DT hotspot must reach high ion temperatures, T_{ion} >5 keV, and high areal densities, ρr > 0.2–0.3 g/cm^2, to initiate burn, while the total yield depends on the confinement time provided by the total areal density of the DT and remaining ablator, typically designed at 1–2 g/cm^2.

The goal of the National Ignition Facility (NIF) is to increase the liberated fusion energy "yield" in inertial confinement fusion (ICF) experiments well past the ignition threshold and the input laser energy. Most recent efforts have focused on increasing the capsule size to increase the capsule absorbed energy and this paper follows in this vein using a frustraum[3] to drive a 1.2 mm inner radius HDC capsule and setting the record for the maximum capsule absorbed energy achieved on the NIF. This large capsule size in a relatively large frustraum, however, results in longer coast times, >1.5 ns, which affects the performance of the implosions.

In Sec. II, we review the experimental parameters from the frustraum campaign in which a frustraum that measured 9.76 mm in diameter at the capsule equator by 12.24 mm in length with 23° wall angles was used to drive most of the implosions. In Section III, we discuss the experiments conducted to test several methods to control the capsule symmetry in preparation for layered implosions. In Section IV, we discuss the two layered implosions carried out in the platform. We compare the frustraum to the other campaigns utilizing HDC ablators on the NIF to better understand the effects of capsule absorbed energy, dopant level and coast time on the performance of these implosions. We also derive generalized Lawson criteria which enable us to define a minimum yield and ion temperature as a function of coast time necessary to reach ignition and

indicate how far these frustraum-driven implosions are from reaching ignition. In Sec. V we summarize the results of this Frustraum platform and describe potential improvements to increase the performance of this platform in the future.

II. EXPERIMENTAL DETAILS

The hohlraum configuration used in the experiments described in this article was a frustraum[3] geometry as shown in Figure 1. The frustraum used to drive these experiments, in all but one experiment, measured 9.76 mm in diameter at the capsule equator and was 12.24 mm in length. These hohlraums were built with 23° wall angles with a wall area A_{wall} = 270 mm^2, and had a laser entrance hole "LEH" that was 3.1 mm in diameter on either end of the frustraum. The wall area for these frustraum are slightly more than the 6.4 mm diameter by 11.3 mm long cylindrical hohlraum used in the HyE campaigns, A_{wall} = 257 mm^2 The wall material for the hohlraums were either gold or gold-lined uranium, primarily dependent on the laser energy of the experiment. The HDC capsules placed in the center of the frustraum had an inner radius of 1.2 mm and an overall HDC ablator shell thickness of ~81 μm. The capsules consisted of a clean HDC layer on the inside of the shell followed by a doped layer which contained 0.35% W dopant. The outer layer of the shell was again composed of clean HDC material. The symmetry and 2D-ConA experiments described below primarily used capsules that were filled with deuterium at 1817 Torr or a mixture of 67%/33% D3He at 2164 Torr to give an initial mass density inside the capsule of 4 mg/cm^3 at the fielding temperature of 32^o K. In all cases the frustraums were filled with 0.3 mg/cm^3 of He gas. The implosions were driven by a three-level laser pulse shape that generated three levels of x-ray drive in the hohlraum and x-ray ablation pressure on the capsules, sending three primary shocks into the HDC ablator.

III. SYMMETRY CONTROL EXPERIMENTS

a. P2 sensitivity

Experiments were conducted to determine the sensitivity of the platform to various methods used to control P2 mode asymmetry. One technique is through the use of inner beam cone fraction, defined as the energy in the inner cones vs. the total laser energy. While this technique is useful in the foot and second level of the laser pulse, when it is used in the peak it prevents full delivery of the laser energy to the target. We conducted experiments to test other methods to control the capsule drive symmetry in the peak of the laser pulse.

i. Wavelength separation between the inner and outer cones

One technique that is commonly used to change the P2 drive asymmetry for implosions on the NIF is to change the wavelength between the inner and outer beams[4] which changes the level of cross beam energy transfer "CBET" between cones of beams. To move more energy from the outer beams to the inner beams the wavelength of the inner beams is typically set to a longer wavelength than the outer beams. As the wavelength difference is increased, more energy is transferred from the outer cones to the inner cones driving the equator of the capsule and making the P2 mode more positive. To determine the sensitivity of this method for controlling P2 in the frustraum a pair of implosion experiments were conducted, N200108 and N211017, with a change in the wavelength between the inner and outer beams. N200108 had the same wavelength on both the inner and outer beams and measured the hotspot shape at the implosion's stagnation time. N211017 had a wavelength separation of 0.5 Å between the inner and outer beams and this experiment radiographed the ablator shell as it was imploding, as well as, measuring the hotspot shape at the implosion's stagnation time. As shown in Fig. 2 both implosions had the same average stagnated radius P0 = 83 μm while P2 increased from -1 μm to 24 μm with the application of 0.5

Å longer wavelength on the inners. Taking into account the differences in inner beam cone fraction at peak power, the measured P2 sensitivity was ~ 44 μm/Å. One other difference between the two experiments was that N211017 used a gold-lined DU frustraum and N200108 used a gold frustraum. These configurations behave the same in the foot and second level of the pulse but the gold-lined DU frustraum reaches a higher effective peak power, ~6.5%, due to the higher wall albedo when the Marshak wave breaks through the 700 nm thick gold liner. Direct A:B experiments in the BigFoot campaign, however, indicated that there was no meaningful change in P2 between gold and gold-lined DU hohlraums(N180128 and N180930).

ii. Outer cone pointing change

Another technique that has been successful in changing P2 in cylindrical hohlraums is to change the outer beam pointing as shown in Fig. 3a. Moving the outer beams closer to the capsule makes the P2 mode more positive and moving it closer to the LEH to makes it more negative. To determine the sensitivity of this method of controlling P2 in the frustraum two pairs of implosions were conducted, N200108 and N200217, with a change in the z (along the frustraum axis) outer beam pointing of 200 μm and N200721 and N201018 with a change in the outer beam pointing of 100 μm. Fig. 3b shows the hotspot shapes for N200108 and N200217 which both used the same laser pulse shape, symmetry platform, wavelength and frustraum wall material. Accounting for changes in the inner beam cone fraction this pair of experiments resulted in a P2 change of 24 μm or ~12 μm/100 μm pointing change in the outer beams.

Fig. 3b also shows the hotspot shapes for N200721 and N201018 which both used the same laser pulse shape, symmetry platform and frustraum wall material. One difference in this pair was that N201018 had a 0.4A shift between the 44.5 and 50 degree cones with the inner beams set to

the average of these two wavelengths. The reason for this is that in the majority of the campaigns on the NIF the highest levels of SBS are driven by the 50 degree outer cones. This can be mitigated by imposing a small wavelength between the two outer cones, typically, 0.4 Å, which transfers energy from the 50 degree outer cones to the 44.5 degree outer cones to reduce the SBS levels on the 50 degree beams and increase it slightly on the 44.5 degree beams.[5] This was applied as the laser energy was increased to ensure that the platform could reach high laser energies without driving damaging levels of SBS, > 1 J/cm^2. Accounting for changes in the inner beam cone fraction, this pair of experiments resulted in a P2 change of 7 μm/100 μm pointing change in the outer beams, however, the four color wavelength present in N201018 made this experiment slightly more prolate than it otherwise would have been such that this latter pair of experiments is also consistent with a pointing change sensitivity of 10 to 12 μm/100 μm pointing change in the outer beams.

iii. Wall angle change

Another technique that can be used in a frustraum to change the P2 mode is to alter the angle of the walls themselves. To determine the sensitivity of this method of controlling P2 in the frustraum a pair of implosions were conducted, N210608 and N210724, with a change in the wall angle of the frustraum between the two shots. The geometry for the experiments is shown in Fig. 4a with N210608 and N210724 performed in frustraums with a 23° (red) and 25° (black)wall angle respectively. The increase in wall angle reduces the intensity of the outer beams on the wall 12% reducing the gold bubble velocity. It also moves the outer beam spots closer to the midplane and at a larger radius, providing more drive to the capsule equator. The effective pointing change of the outer beams for the two degree increases in the wall angle is -0.13 mm in z and +5° in spot angle subtended to capsule with respect to the laser axis. The increase in wall angle also

changesthe plasma flow direction from the wall which is then predicted to increase the cross-beam-energy-transfer from the outer to inner beams for the case of a positive $\Delta\lambda$.. As seen in Fig. 4, increasing the wall angle by two degrees \increased the core P2 measured from neutron imaging by 45 μm. The ΔP2 has been corrected by -15 μm for a known mode 1 residual hot spot velocity on each of the shots. . From the preceding section, the -0.13 mm pointing change would represent a modest change in P2, +16 μm, with the remaining +29 μm attributed to reduction in impairment of inner beam transport by the gold bubble from the reduced fluence on the wall and increase is =CBET

iv. Empirical Mode P2 Sensitivity

Previous papers have used empirical models to characterize and predict the P2 shape in cylindrical hohlraums.[6, 7] A series of 14 experiments measuring shape were carried out in different frustraum configurations which included wall angles of 21, 23 and 25 degrees, diameters at the equator of the capsule of 7, 9.26 and 9.76 mm and capsule inner radii of 1050, 1200 and 1400 μm, In a similar fashion to cylindrical hohlraum empirical models, we have placed the 14 frustraum experiments in a similar plot with the P2 at 33% cone fraction divided by $M^{1.5}=R_{cap}/CCR^{0.5}$ along the y axis and along the x-axis as the expression $\mathrm{sqrt}(E_{out}/A/\rho)(\tau/R_{hohl})(CCR)$. expression E_{out} is the energy in the picket of the outer beams, A is the area of the outer beams, ρ is the density of the hohlraum gas, τ is the time between the beginning and the middle of the peak power of the outer beam, R_{hohl} is the radius where the 50 degree beams intersect the frustraum wall, CCR is the minimum case-to-ratio, the outer radius of the capsule, r_{cap}, divided by the closest radius of the frustraum to the capsule surface. The y value is calculated using the measured P2(μm)/$M^{1.5}$ and then subtracting off the changes in P2. The first change subtracted off is due to the peak cone fraction difference from 33%, -100*(0.33-CF)*3.5. Another change in P2 is due to cross beam

energy transfer between the inner and outer cones, -(δλ in A)*30 μm/A. The final change in the P2 is due to the outer beam spot motion from the initial average outer beam spot angle, θ_{init}, to the average outer beam spot angle at peak power, θ_{pp}, -6.5(θ_{pp}- 48.6). For this latter change we assume that the walls are moving radially inward at ~71 μm/ns and the value of 48.6 is just used to move all of the data points along the y axis. In this As in the case of cylindrical hohlraums most points fall along a line in this phase space. The largest outlier is the one experiment conducted with a 25 degree wall angle on the frustraum, which resulted a large change in P2, ~59 μm.

v. Smoothing effects of the large case-to-capsule ratio

The frustraum has a large diameter at the equator relative to cylindrical hohlraums and thus perturbations on the wall are smoothed relative to cylinder due to the smaller solid angle of the perturbation on the capsule. This can be examined by comparing the perturbation caused by the two uncoated diagnostic windows in the convergent ablator experiments which are carried out in each platform on the NIF. The windows are uncoated HDC, 800 μm by 800 μm in size and placed 180 deg. apart on the hohlraum wall. Looking from the pole these two windows cause an M2 mode to be generated on the capsule implosion due to the local reduction in the x-ray drive along the axis of the two diagnostic windows. Fig. 6a shows a plot of the hotspot M0 vs the initial capsule radius across a number of platforms. The frustraum is represented by the 1200 μm inner radius point. Fig. 6b shows the M2/M0 of the hotspot caused by the window perturbation as a function of the initial solid angle of the window on the capsule. The frustraum represents the smallest M2/M0 perturbation on the capsule due to its large CCR. There is roughly a linear effect with window solid angle on capsule hotspot M2/M0.

b. Reduction of systematic Mode 1 perturbations in the hohlraum

Mode 1 also degrades the performance of layered implosions and has numerous sources. [8, 9] These sources include a mode 1 driven by the as delivered laser energy or beam pointing, mode 1 variations in the capsule and ice thickness, and a miscentered capsule in the hohlraum.[10] Until recently most layered implosions were carried out in hohlraums with diagnostic windows which introduced a systematic mode 1 in all of these implosions. The second frustraum layered implosion, N210725, incorporated three diagnostic windows into the hohlraum with the placement of the windows in azimuth chosen to mitigate this systematic mode 1 perturbation that had been present in previous layered implosions.

c. P4 effects

The experimental x-ray self-emission images from symmetry capsule, symcap, experiments show a feature that is reminiscent of the tent features seen in implosions with GDP capsules.[11-13] These features are, however, also seen in hohlraum simulations with no tent present. For these experiments the z pointing of the 44 cone was further away from the capsule than the 50 degree cone which increased the P4 in these experiments. In the simulations this feature is due to the P4 in combination with a higher growth factor in the design. In the experiments this feature is likely due mostly to the P4 but in combination with the tent and the higher growth factors of the design. Fig. 7 shows images of the hotspot as a function of time with time progressing from left to right. In these images we see the propagation of two lines on the top and bottom of the hotspot penetrating further into the hotspot as a function of time. The outer edge of the hotspot provides a measure of the hotspot x-ray M0, from which we can deduce the center of the hotspot and the distance between the center of the hotspot and the leading edge of emission attributed to the P4/tent feature. The time dependences of M0 and radius are plotted in Fig 7b and 7c, where the radius is the distance from the center of the hotspot to the inner radius of either line on the top and bottom.

We can then use models to reproduce the experimental observations of the motion of the P4 feature into the hotspot and infer the mass injected into the hotspot from these P4 features. We implemented two models to reproduce the P4 feature trajectory through the hotspot and in both models make the simplifying assumption that the injected mass and cross-sectional area are not changing with time and the hotspot density is uniform inside the hotspot but varies in time. The first model is a snow-plow model that can be expressed by the equation

$$M_s V_s = (M_s + \beta\rho(t)Az(t))\frac{dz(t)}{dt} \quad (1$$

where β is a parameter that allows some of the mass to not be accumulated, ρ is hotspot density, A is the area of the injected jet, M_s is the initial mass of the injected jet, V_s is the initial velocity of the injected jet and z is the position of the edge of the jet relative to the center of the hotspot. The time-dependent mass of the jet feature is given by $M_s + \beta\rho(t)Az(t)$, where M_s is the initial mass and $\beta\rho(t)Az(t)$ is the additional accumulated mass. The only time-dependent quantities in this equation are ρ and z with the initial value of $z(t_{init})=0$ and the initial value of $\frac{dz}{dt}(t_{init}) = V_s$. The only change from a traditional snow-plow model[14, 15] is the addition of the β term that allows only a portion of the hotspot mass to be swept up given that the time over which the feature travels through the hotspot is larger than its cross-sectional radius divided by the sound speed. The total accumulated mass in this model is then given by βρAΔr, where Δr is the distance traveled through the hotspot. The second model is a drag model which can be expressed by the equation[15, 16]

$$M_s \frac{dV_s}{dt} = C_D A\rho V_s^2/2 \quad (2$$

where M_s is the initial mass, V_s is the velocity of the jet coming from the fill tube, A is the area of the jet, ρ is the mass density of the hotspot and C_D is the drag coefficient slowing down the jet of

material. The hotspot density is changing rapidly as the hotspot is being compressed by the ablator and it can be fit with a simple polynomial, $\rho = \rho(0) + Bt + Dt^2$, to enable an analytic form for the velocity of the feature in the hotspot

$$V_s(t) = V_s(0)/(1-C_D A V_s(0)(\rho(0)t+0.5Bt^2+0.33Dt^3)/(2M_s)). \quad (3$$

Other models have been developed to infer the level of high-Z material mixed into the hotspot of layered implosions.[17] This model measures the total level of mix into the hotspot and assumes all of the x-ray emission comes from the hotspot. As such this model is not typically used for symcap implosions as discussed in this article where the majority of the x-ray emission can come from the ablator. Likewise this model assumes that the mix is in thermal equilibrium with the hotspot which recent work has disputed.[18] The models presented in this paper do not rely on whether the mix is in thermal equilibrium with the hotspot, whether the x-ray emission is only coming from the hotspot and not the ablator, they do not require nuclear yield data and they can look directly at the mix entering the hotspot from the feature causing the mix.

Both the snow plow and drag models were applied to the data in the top row of Fig. 7 to determine the quantities, A, M_s, V_s, r(t) and ρ(t) in Eqs. 1 and 2. These values of the parameter β in the snow-plow model and C_D in the drag model used in Fig. 7b and 7c were β = 0.44 and C_D = 1. The snow-plow model is shown by the dashed black line in Fig. 7b and the drag model is shown by the dashed black line in Fig. 7c. The level of injected mass estimated by these two models is approximately 350 ng per horizontal feature.

IV. LAYERED IMPLOSIONS

a. Frustraum Implosion Results

In this frustraum campaign, two layered implosions were carried out on the NIF. These layered implosions had a high design adiabat, α~4.6, higher than the previous BigFoot platform(α~4). This was due to the first shock entering the DT fuel at ~41 km/sec and the second merged shock reaching 72 km/sec and merging with the first shock ~half way into the ice layer, as opposed to the BigFoot campaign which merged the first and second shocks just before the ice layer and had the combined first and second shocks enter the ice at ~50 km/sec. The two frustraum layered implosions were conducted at two different laser energies, which enabled a further test of the effects of coast time on the implosion performance, as has been done previously. [8, 19-23] The coast time is defined as the time between the point at which the end of the laser pulse reaches half of its peak power and the bang time of the implosion. The pulse shapes used for the two experiments are shown in Fig. 8 along with the bang times to show the difference in coast times between the two experiments. As listed in table 1 the first layered implosions had a 58.6 μm thick ice layer and the second had a 50 μm thick ice layer which also contributed to the change in coast time. The lower energy implosion, the black pulse shape in Fig. 8, had a coast time of 2.17 ns and the higher energy implosion, the red pulse shape in Fig. 8, had a coast time of 1.75 ns. For the second implosion the peak power of the laser pulse was also reduced relative to the first layered implosion and that energy placed at the end of the pulse to further extend the pulse length and reduce the coast time. This technique has been used prior to N210725[20] and subsequently on the N210808 shot[24] which was the first shot on the NIF to achieve ignition.

A summary of the shot performance is given in Table 1 for both of the frustraum shots, as well as the best performing shots in the BigFoot, HDC and HyE1100 campaigns. The hotspot neutron images measured for the two frustraum layered implosions are seen in Fig. 9. The first implosion was nearly round with a P0 of 45 μm and a P2 of 4.5 μm. The second implosion was

oblate with a P0 of 46 μm and a P2 of -21 μm. The upper right shows the fluence compensated hotspot images in the top left corners. Looking at all of the shots listed in Table 1 we see a monotonic increase in hotspot size, P0, capsule absorbed energy, burn width and hotspot energy with initial capsule diameter. Likewise, as the initial capsule radius increases, we see a decrease in the hotspot pressure, yield amplification and ion temperature across most of the campaigns.

b. Hohlraum Cooling and Coast Time

To isolate the effects of coast time on implosion compression and performance, it has been recognized that this is tied to the hohlraum cooling time after the laser is off. [8, 19-23] With a few simplifying assumptions we can calculate the time dependence of the hohlraum radiation temperature once the laser is turned off. [25] The energy stored in the hohlraum wall during the time that the laser is at peak power can be approximated as $E_{wall} \cong \sigma T_r^4(t') A_{wall}(1 - a_{wall}) t_p$ where t_p is the time duration over which the laser is at peak power. To approximate the time dependance of the hohlraum radiation temperature once the laser is turned off, we can set the change in energy stored in the wall over a time Δt, $\left(T_r^4(t' + \Delta t) - T_r^4(t')\right)\sigma A_{wall}(1 - a_{wall}) t_p$, equal to the energy lost to radiation exiting the LEHs and absorbed by the capsule, $\sigma T_r^4(t)\left(A_{leh} + A_{cap}\left(1 - a_{cap}\right)\right)\Delta t$, and the energy lost to heating deeper into wall, $\sigma T_r^4(t) A_{wall}(1 - a_{wall})\Delta t$, such that:

$$\frac{1}{T_r^4(t)} \frac{dT_r^4(t)}{dt} = -\frac{A_{leh} + A_{cap}\left(1 - a_{cap}\right) + A_{wall}(1 - a_{wall})}{A_{wall}(1 - a_{wall}) t_p} \qquad (4$$

where T_r is the radiation temperature of the cavity, A_{leh} is the total area of both laser entrance holes, A_{cap} and α_{cap} are the area and albedo of the capsule after the laser is turned off, , and A_{wall} and α_{wall} are the area and flux weighted time-averaged albedo of the wall during peak power . If we ignore

the time dependence after laser is turned off in each of the terms on the right-hand side of the equation, then the solution is simply

$$T_r^4(t) = T_r^4(t_p)e^{\frac{-(A_{leh}+A_{cap}(1-a_{cap})+A_{wall}(1-a_{wall})t)}{A_{wall}(1-a_{wall})t_0}} = T_r^4(t_p)e^{\frac{-t}{t_{cool}}} \quad (5$$

where $t_{cool} = \frac{A_{wall}(1-a_{wall})t_p}{A_{leh}+A_{cap}(1-a_{cap})+A_{wall}(1-a_{wall})} \approx \frac{t_p}{1+A_{leh}/A_{wall}(1-a_{wall})}$.

and the last expression recognizes that the capsule area has greatly shrunk by the time the laser drive is off. One can derive the average albedo of the wall, α_{wall}, for the usual case of a constant peak power pulse for which T_r rises as $t^{0.115}$. [26] The time average of the wall loss, $T_r^4(1 - \alpha_{wall})$, gives a $\alpha_{wall} = 1 - 0.66/(T_r^{0.7}t_p^{0.38})$ for Au with T_r at the end of the laser drive in hectoelectron volts and t_p in ns. [26] For the higher albedo unlined or Au-lined DU based hohlraums [27] used for most of the DT shots, the 0.66 factor reduces to 0.5 and 0.55, respectively, at $T_r = 3$ heV. So, for example, for the Au-lined DU frustraum shot N210117 with peak $T_r = 2.9$ heV, $t_p = 1.8$ ns and $(A_{leh} + A_{cap}(1-\alpha_{cap}))/A_{wall} = .05$, $\alpha_{wall} = 0.83$ and $t_{cool} = 1.4$ ns. This analytic estimate of the time dependent flux(blue) agrees very well with the measured flux for N210117(green) shown in Fig. 8.

c. Stagnated Areal Density

The effect of coast time on the DSR/(μm of ice) is shown in Figs. 10a and b. This includes all of the campaigns on the NIF that used HDC ablators: BigFoot[28-40], HDC[41-46], Iraum[47, 48], HyB[49, 50], HyE 1100[51, 52] and HyE 1050[24, 53, 54] campaigns, as well as the frustraum shots represented by the black points. The bubble size reflects the dopant areal density ρΔR in units of %μm present in the capsules, where bubble size= $1000(\rho\Delta R)^2 + 0.5$ In Fig. 10b, the DSR values have been slightly corrected based on fits to simulations for yield amplification, DSR_{cor} =

$DSR_{meas}/(0.55+0.45*\exp((1-Y_{amp})/20))$, for P2 and for P1, $DSR_{cor} = DSR_{meas}/(1-DSR_{M1}^2)$. The P2 correction assumes DSR for a given fuel mass and volume scales as $Volume^{2/3}/(\text{surface area})$ approximating surface area-to-volume ratios using oblate and prolate spheroids, that fit DSR vs downscattered NI P2/P0 in simulations. This can be fit by the expression $DSR_{cor} = DSR_{meas}/(1+\chi*(3*(P2/P0)/(4+(P2/P0)))^2)$, where the value of $\chi = 0.69$ is used for prolate implosions and increases to $\chi = 0.84$ for oblate implosions. Plotted in this fashion it is clear that all of the HDC campaigns to date, with coast times > 1 ns, are limited in their maximum achievable DSR by their coast time. Fig. 10 also shows that the maximum DSR and hence effective minimum stagnation adiabat of HDC-based implosions is approximately constant for a given coast time across all campaigns as noted previously. [55] So it is fair to fit the envelope of all campaigns as one universal curve versus coast time, ignoring small variations in t_{cool}. The envelope fit as shown in Fig. 10a can be expressed as $DSR/(\mu m \text{ of DT ice}) = 0.145\exp(-t_{coast}/1.8)\ \%/\mu m$ [56] Coast time effects saturate in simulations as the coast time of the implosions becomes smaller than the sum of the sound crossing time in the capsule and the deceleration time of the implosion, ~1 ns.[57] This is apparent in Fig. 10 where we can see that the BigFoot campaign, for instance, has an approximately constant peak DSR/(μm of ice) for coast times less than ~ 1.2 ns.

To relate t_{cool} to the effects of t_{coast}, an analytic model[56] was developed to relate the stagnated fuel areal density that is inferred from the neutron downscattered ratio (DSR) to t_{coast}. We can derive a simplified version of this relationship. For adiabatic deceleration of the shell we have the expression

$$P_s R_{hs}^5 = \alpha_{hs} M_{hs}^{5/3}, \quad (6$$

Where P_s is the pressure in the DT shell, R_{hs} is the hotspot radius, α_{hs} is the adiabat of the hotspot and M_{hs} is the mass of the hotspot. We assume a pressure equilibrium between the shell and the

hotspot, P_{hs}, at stagnation such that $P_s \sim P_{hs}$. The outer DT shell radius at stagnation, R_s, is assumed to be proportional to the hotspot radius, $R_s = \beta R_{hs}$, where β is greater than one and varies depending on the level of mix in the fuel. We assume an energy balance between the material inside the outer radius of the shell at stagnation, $P_s R_s^3$, and the peak kinetic energy in the fuel, $M_f V_{imp}^2$

$$P_s R_s^3 \propto M_f v_{imp}^2 \quad (7$$

Where M_f is the initial mass of the DT fuel shell and v_{imp} is the peak implosion velocity. We can substitute eq. 7 into eq.6 and arrive at the expression

$$\frac{R_i^2}{R_s^2}\frac{1}{d_i} = \frac{v_{imp}^2}{\alpha_{hs} M_{hs}^{5/3}}\frac{\rho_i R_i^4}{\beta} \quad (8$$

Where R_i is the inner radius of the ablator, d_i is the initial thickness of the DT ice layer and ρ_i is the initial density of the ice layer, 0.255 g/cm^2. Using mass conservation we can equate the initial mass in the DT shell, $M_f = 4\pi\rho_i R_i^2 d_i$ and the vapor $(4/3)\pi\rho_g R_i^3$ with the mass in the shell at stagnation, $4_p\rho_s R_s^2 d_s$, and the mass in the hotspot, $(4/3)\pi\rho_{hs} R_{hs}^3$. The downscattered ratio, DSR, is proportional to the areal density of the DT or DSR ~ $\rho s d s + (\rho_{hs} R_{hs})/(3\beta^{2/5})$ and hence

$$\frac{DSR}{d_i} \sim \left(\frac{R_i}{R_s}\right)^2 \left(\rho_i + \frac{\rho_g R_i}{3 d_i}\right) \sim \left(\frac{R_i}{R_s}\right)^2 \rho_i \quad (9$$

Inserting eq. 9 into eq. 8 then allows us to relate the DSR to the peak implosion velocity, the hotspot adiabat and the hotspot mass

$$\frac{DSR}{d_i} \sim \frac{v_{imp}^2}{\alpha_{hs} M_{hs}^{5/3}}\frac{\rho_i R_i^4}{\beta}. \quad (10$$

The hotspot mass includes both the initial vapor inside the shell, $(4/3)\pi\rho_g R_i^3$, as well as a portion of the initial shell which we will write as $M_f f(Y_{amp})$ to indicate that this can be expressed as a function of the yield amplification, Y_{amp}, of the implosion and results in a decrease in DSR as the yield amplification increases.

In [56] the authors used a Rocket model to relate the peak implosion velocity to the hohlraum's radiation temperature at peak velocity. We have taken this same approach to model N210117 and variations of N210117 which change the time duration that the laser was at peak power in order to vary the coast time of the implosion and the radiation temperature at peak implosion velocity, T_{rpv}. The results of this series of rocket model simulations is shown in Fig. 8b which shows the coast time and peak implosion velocity as a function of T_{rpv}. For the coast times relevant to the current two frustraum shots, ~1.2 to 2.2 ns, the peak implosion velocity as a function of the radiation temperature at peak velocity can be fit to a power law, $v_{imp} \sim T_{rpv}^{0.9}$. As such the DSR can be expressed as DSR ~ $(v_{imp}^2/ \alpha_s) = (T_r^{1.8}/ \alpha_s)$, or with the t_{cool} = 1.4 ns for N210117 DSR ~ $(T_r(0)^{1.8}/\alpha_s)\exp(-1.8t/4t_{cool})$. This agrees reasonably well with the empirical fit to the NIF data shown in Fig. 10a given in the preceding paragraph.

d. Hot Spot Performance

The large inner radius of the frustraum capsules, 1200 μm, allows them to absorb large amounts of energy, >250 kJ for N210725, even with the relatively low laser energy of 1.74 MJ. The capsule absorbed energies for the different implosions is seen in Fig. 11 where the bubble size for this plot is proportional to the yield amplification of the implosion and again the two frustraum implosions are represented by the black circles. From this figure we can see that even though the capsule absorbed energy is higher, the yield amplification remains fairly low, ~2, at these large coast times, similar to the HyE1100[51, 52] campaign results.

Figure 12a shows the primary yield achieved for each of the HDC layered implosions as a function of coast time. Figure 12b normalizes the yield by the inner capsule radius to the 4.5 power

and the coast time by the capsule inner radius. The bubble size for this plot is proportional to the capsule inner radius, bubble size = $(R_{cap})^5$, of the implosion and again the two frustraum implosions are represented by the black circles and represent the largest two capsules used for indirect-drive layered implosions on the NIF. The larger capsule radius and the large hohlraum size, however, contributes to the higher coast times for these implosions. The yield for the two frustraum layered implosions is similar to the maximum yield obtained in other HDC campaigns such as the BigFoot[29-40], HDC[41-46] and Hy1100[51, 52] campaigns which all had a maximum yield of ~$2x10^{16}$ neutrons. Correcting the shape of the N210725 layered implosion could increase the yield to perhaps $3x10^{16}$. The implosions using 1200 μm I.R. capsules in the frustraum campaign, like the implosions using 1100 μm I.R. capsules used in the HyE campaign tended to have higher hotspot energies and lower pressures and yield amplifications than seen in the HDC(910 μm I.R. capsules) and BigFoot(950 μm I.R. capsules) campaigns even though they all achieved similar yields.

As reported in [32] the ignition threshold factor can be used to formulate a generalized Lawson criteria, GLC, for ignition which includes alpha heating and uses only the directly measured quantities of DSR, primary neutron yield, $Y_{13\text{-}15}$, and the initial ice mass, M_{fuel}. In [32] this GLC was defined as GLC(ITFXmod) = $0.27(\text{ITFXmod})^{0.6}$, with ITFXmod ~ $(19.7*\text{DSR})^2*(0.24*(4f_Df_T)*Y_{13\text{-}15}/(M_{fuel}))$. Fig. 13a shows GLC(ITFXmod) plotted against GLC = $(P_{stag}/420)(E_{hs}/30)^{0.5}$. With GLC(ITFXmod) used in conjunction with the empirical fit of the maximum DSR vs. time seen in Fig. 10a, the minimum yield as a function of coast time can be defined based on these quantities. The dashed line in Fig. 12 shows this minimum yield required for ignition as a function of coast time. It should be noted that all implosions with coast times less than ~1 ns and many shots with coast times >1ns have DSRs lower than the demarcation line. For these implosions the yields required to satisfy GLC(ITFXmod) are higher than the dashed line in

Fig. 12. The dashed line in Fig. 12 could therefore be thought of as a necessary but not sufficient condition for ignition. A GLC with T_{ion} and DSR can also be formulated from GLC(ITFXmod) by substituting the yield dependence on DSR and temperature, similar to Eq. 39 of [58], $Y \alpha (M_{fuel}) DSR^{0.583}(T_{ion})^{5.83}$, into ITFXmod or GLC(DSR, T_{ion}) = $(0.187)DSR^{1.55}Tion^{3.5}$ as shown in Fig. 13b. There is more uncertainty in this definition of GLC than in the GLC(ITFXmod) but it allows us to use the demarcation line in DSR along with GLC(DSR, T_{ion}) to determine a minimum T_{ion} vs. coast time for ignition which is then plotted in Fig. 14.

Fig. 14 shows the ion temperature from all of the HDC layered DT implosions conducted on the NIF. Again, the two frustraum implosions are represented by the black circles. The bubble size reflects the dopant areal density as in Fig. 10. The larger hotspot size, due to the larger initial capsule radius and the long coast time affecting the compression, results in ion temperatures that are slightly lower than in the HyE1100 campaign. The dashed line in Fig. 14 represents the minimum T_{ion} required to reach ignition as a function of coast time. Again it should be noted that all implosions with coast times less than ~1 ns and many implosions with coast times > 1 ns have DSRs lower than the demarcation line and so the ion temperatures required to satisfy GLC(DSR, T_{ion}) for those implosions are higher than the dashed line in Fig. 14.

V. SUMMARY

Most efforts to improve performance of layered implosions to date have focused on increasing the capsule size to increase the surface area and the capsule absorbed energy. In this article we extend this approach by fielding the largest HDC capsules, 1.2 mm inner radius, to date for indirect-drive inertial confinement fusion. Even at 1.74 MJ of laser energy this surpassed the previous indirect-drive capsule absorbed energies achieved in layered implosions on the NIF.

These larger capsules and frustraum sizes with the limited energy available on the NIF, however, resulted in long coast times, $\geq$1.75 ns. The long coast times reduced the hohlraum drive onto the capsule by the time of peak compression and resulted in lower DSR values. We presented the results of these implosions along with all of the HDC layered implosions conducted on the NIF. This allowed us to conclude that by looking at the DSR vs. coast time results that there is a maximum achievable DSR for all of the HDC campaigns on the NIF, including the frustraum campaign. The maximum DSR/(μm of DT ice) across the different campaigns was found to be expressed as DSR/(μm of DT ice) = $0.15\exp(-0.56*t_{coast})$ %/μm and for the long coast times in the frustraum layered implosions, both experiments fell close to this line. We previously derived a generalized Lawson criterion based on the ignition threshold factor and used that in conjunction with maximum DSR as a function of coast time to derive a minimum yield required for ignition as a function of coast time. Similarly, we put the yield in terms of DSR and T_{ion} which allowed us to derive minimum ion temperature as a function of coast time for ignition as well.

We are in the process of improving the performance of this platform by reducing the overall size of the Frustraum by ~15% and the capsule diameter by 9%, 1.1 mm I.R., to enable higher radiation drive and shorter coast times, ~1 ns. In addition, the laser pulse shape is adjusted to reduce the design adiabat of the implosions from >4 in the current platform to <3 to increase the DSR of the implosions. We have also moved the 44.5 deg cone closer to the capsule and the 50 deg. cone further away to reduce the level of P4 seen in the current platform and we will report on this work in a later article.

ACKNOWLEDGMENTS

We wish to thank the NIF operations team. This work was performed under the auspices of the U.S. Department of Energy by Lawrence Livermore National Laboratory under Contract DE-AC52-07NA27344 and by General Atomics under contract DE-NA0001808. The data that support the findings of this study are available from the corresponding author upon reasonable request. This document was prepared as an account of work sponsored by an agency of the United States government. Neither the United States government nor Lawrence Livermore National Security, LLC, nor any of their employees makes any warranty, expressed or implied, or assumes any legal liability or responsibility for the accuracy, completeness, or usefulness of any information, apparatus, product, or process disclosed, or represents that its use would not infringe privately owned rights. Reference herein to any specific commercial product, process, or service by trade name, trademark, manufacturer, or otherwise does not necessarily constitute or imply its endorsement, recommendation, or favoring by the United States government or Lawrence Livermore National Security, LLC. The views and opinions of authors expressed herein do not necessarily state or reflect those of the United States government or Lawrence Livermore National Security, LLC, and shall not be used for advertising or product endorsement purposes.

Appendix A Mode 2 correction for the down-scattered ratio, DSR

The mode P2 degradation of the DSR for a given fuel mass and volume scales as Volume$^{2/3}$/(surface area). One can approximate the surface area-to-volume ratios analytically using oblate and prolate spheroids and relate the Legendre polynomials to the equatorial and polar radius of the spheroid. For a spheroid with the z-axis representing the symmetry axis, the cartesian equation describing the surface is given as

$$\frac{x^2+y^2}{a^2}+\frac{z^2}{c^2}=1. \quad (1$$

For a prolate ellipsoid, c>a, the surface area is given by

$$2\pi a^2\left(1+\frac{(c/a)^2}{\sqrt{(c/a)^2-1}}\sin^{-1}\sqrt{1-(a/c)^2}\right) \quad (2$$

and for an oblate ellipsoid, a>c, the surface area is

$$2\pi a^2\left(1+\frac{(c/a)^2}{\sqrt{1-(c/a)^2}}ln\left(\frac{1+\sqrt{1-(c/a)^2}}{1-\sqrt{1-(c/a)^2}}\right)\right). \quad (3$$

The volume of an ellipsod is expressed as

$$\frac{4}{3}\pi a^2 c \quad (4$$

The radii of the ellipsoid are related to the Legendre modes P2/P0 through the relation[59]

$$\frac{c}{a}=\frac{1+^{P2}/_{P0}}{1-0.5(^{P2}/_{P0})}. \quad (5$$

We can then compare the analytic expression of the DSR degradation, Volume$^{2/3}$/(surface area), dashed red line, to the downscattered DSR vs. NI P2/P0 seen in simulations, black circles, as shown

in Figure 15. We can also fit a simplified expression to the simulations and the Volume$^{2/3}$/(surface area), which is what we use in the paper to correct the DSR to mode 2. This fit, blue line, is shown in Fig. 15 and is expressed as (1+χ*(3*(P2/P0)/(4+(P2/P0)))^2), where the value of χ = 0.69 is used for prolate implosions and increases to χ = 0.84 for oblate implosions.

REFERENCES

1. J. Lindl, Phys. Plasmas **2** (11), 3933-4024 (1995).

2. S. Atzeni and J. Meyer-ter-Vehn, *The Physics of Inertial Fusion*. (Oxford University Press, 2008).

3. P. Amendt, D. Ho, Y. Ping, V. Smalyuk, S. Khan, J. Lindl, D. Strozzi, R. Tommasini, M. Belyaev, C. Cerjan, O. Jones, W. Kruer, N. Meezan, H. Robey, F. Tsung, C. Weber and C. Young, Physics of Plasmas **26** (8), 082707 (2019).

4. P. Michel, L. Divol, E. A. Williams, others, S. Weber, C. A. Thomas, D. A. Callahan, S. W. Haan, J. D. Salmonson, S. Dixit, D. E. Hinkel, M. J. Edwards, B. J. MacGowan, J. D. Lindl, S. H. Glenzer and L. J. Suter, Phys. Rev. Lett. **102**, 25004 (2009).

5. J. E. Ralph, P. Michel, B. J. MacGowan, D. J. Strozzi, N. B. Meezan, J. M. Di Nicola, J. E. Heebner, V. J. Hernandez, L. Pelz, S. Yang, N. Lemos, L. Divol, A. Kemp, T. Chapman, S. F. Khan, O. L. Landen, J. D. Moody, R. P. J. Town and M. J. Edwards, Physical Review Applied **18** (4), 044040 (2022).

6. D. A. Callahan, O. A. Hurricane, J. E. Ralph, C. A. Thomas, K. L. Baker, L. R. Benedetti, L. F. Berzak Hopkins, D. T. Casey, T. Chapman, C. E. Czajka, E. L. Dewald, L. Divol, T. Döppner, D. E. Hinkel, M. Hohenberger, L. C. Jarrott, S. F. Khan, A. L. Kritcher, O. L. Landen, S. LePape, S. A. MacLaren, L. P. Masse, N. B. Meezan, A. E. Pak, J. D. Salmonson, D. T. Woods, N. Izumi, T. Ma, D. A. Mariscal, S. R. Nagel, J. L. Kline, G. A. Kyrala, E. N. Loomis, S. A. Yi, A. B. Zylstra and S. H. Batha, Physics of Plasmas **25** (5), 056305 (2018).

7. N. Izumi, D. T. Woods, N. B. Meezan, J. D. Moody, O. L. Landen, L. Divol, H. Chen, D. A. Callahan, M. Hohenberger, A. L. Kritcher, D. T. Casey, M. D. Rosen, J. S. Ross, M. B. Schneider, M. J. Edwards and W. W. Hsing, Physics of Plasmas **28** (2), 022706 (2021).

8. O. A. Hurricane and others, Physics of Plasmas **29**, 12703 (2022).

9. D. T. Casey, O. L. Landen, E. Hartouni, R. M. Bionta, K. D. Hahn, P. L. Volegov, D. N. Fittinghoff, V. Geppert-Kleinrath, C. H. Wilde, J. L. Milovich, V. A. Smalyuk, J. E. Field, O. A. Hurricane, A. B. Zylstra, A. L. Kritcher, D. S. Clark, C. V. Young, R. C. Nora, D. A. Callahan, B. J. MacGowan, D. H. Munro, B. K. Spears, J. L. Peterson, J. A. Gaffney, K. D. Humbird, M. K. G. Kruse, A. S. Moore, D. J. Schlossberg, M. Gatu-Johnson and J. A. Frenje, Physics of Plasmas **28** (4) (2021).

10. B. J. MacGowan, O. L. Landen, D. T. Casey, C. V. Young, D. A. Callahan, E. P. Hartouni, R. Hatarik, M. Hohenberger, T. Ma, D. Mariscal, A. Moore, R. Nora, H. G. Rinderknecht, D. Schlossberg and B. M. Van Wonterghem, High Energy Density Physics **40**, 100944 (2021).

11. R. Tommasini, J. E. Field, B. A. Hammel, O. L. Landen, S. W. Haan, C. Aracne-Ruddle, L. R. Benedetti, D. K. Bradley, D. A. Callahan, E. L. Dewald, T. Doeppner, M. J. Edwards, O. A. Hurricane, N. Izumi, O. A. Jones, T. Ma, N. B. Meezan, S. R. Nagel, J. R. Rygg, K. S. Segraves, M. Stadermann, R. J. Strauser and R. P. J. Town, Physics of Plasmas **22**, 056315 (2015).

12. S. R. Nagel, S. W. Haan, J. R. Rygg, M. Barrios, L. R. Benedetti, D. K. Bradley, J. E. Field, B. A. Hammel, N. Izumi, O. S. Jones, S. F. Khan, T. Ma, A. E. Pak, R. Tommasini and R. P. J. Town, Phys. Plasmas **22** (22704), 22704 (2015).

13. V. A. Smalyuk, H. F. Robey, C. L. Alday, P. Amendt, C. Aracne-Ruddle, J. R. Bigelow, T. Bunn, D. T. Casey, K. C. Chen, D. S. Clark, J. P. Cortez, J. Crippen, S. Diaz, M. Farrell, S. Felker, J. E. Field, J. Jaquez, S. Johnson, S. W. Haan, B. A. Hammel, A. V. Hamza, M. O. Havre,

C. Heinbockel, W. W. Hsing, K. Kangas, J. J. Kroll, S. O. Kucheyev, O. L. Landen, X. Lepro-Chavez, A. G. MacPhee, D. A. Martinez, J. Milovich, A. Nikroo, L. A. Pickworth, N. Rice, M. Stadermann, D. Steich and C. R. Weber, Physics of Plasmas **25** (7) (2018).

14. V. Y. Baranov and O. N. Derkach, Phys. Rev. E. **48**, 1324 (1993).

15. K. L. Baker, C. A. Thomas, T. R. Dittrich, O. Landen, G. Kyrala, D. T. Casey, C. R. Weber, J. Milovich, D. T. Woods, M. Schneider, S. F. Khan, B. K. Spears, A. Zylstra, C. Kong, J. Crippen, N. Alfonso, C. B. Yeamans, J. D. Moody, A. S. Moore, N. B. Meezan, A. Pak, D. N. Fittinghoff, P. L. Volegov, O. Hurricane, D. Callahan, P. Patel and P. Amendt, Physics of Plasmas **27** (11) (2020).

16. B. R. Munson, D. F. Young and T. H. Okiishi, *Fundamentals of Fluid Mechanics*, 3rd ed. (John Wiley and Sons, Inc. , 1998).

17. T. Ma, P. K. Patel, N. Izumi, P. T. Springer, M. H. Key, L. J. Atherton, L. R. Benedetti, D. K. Bradley, D. A. Callahan, P. M. Celliers, C. J. Cerjan, D. S. Clark, E. L. Dewald, S. N. Dixit, T. Döppner, D. H. Edgell, R. Epstein, S. Glenn, G. Grim, S. W. Haan, B. A. Hammel, D. Hicks, W. W. Hsing, O. S. Jones, S. F. Khan, J. D. Kilkenny, J. L. Kline, G. A. Kyrala, O. L. Landen, S. Le Pape, B. J. Macgowan, A. J. Mackinnon, A. G. Macphee, N. B. Meezan, J. D. Moody, A. Pak, T. Parham, H.-S. Park, J. E. Ralph, S. P. Regan, B. A. Remington, H. F. Robey, J. S. Ross, B. K. Spears, V. Smalyuk, L. J. Suter, R. Tommasini, R. P. Town, S. V. Weber, J. D. Lindl, M. J. Edwards, S. H. Glenzer and E. I. Moses, Physical Review Letters **111** (2013).

18. B. M. Haines, R. C. Shah, J. M. Smidt, B. J. Albright, T. Cardenas, M. R. Douglas, C. Forrest, V. Y. Glebov, M. A. Gunderson, C. E. Hamilton, K. C. Henderson, Y. Kim, M. N. Lee, T. J. Murphy, J. A. Oertel, R. E. Olson, B. M. Patterson, R. B. Randolph and D. W. Schmidt, Nat. Commun **11**, 544 (2020).

19. H. F. Robey, P. M. Celliers, J. L. Kline, A. J. Mackinnon, T. R. Boehly, O. L. Landen, J. H. Eggert, D. Hicks, S. L. Pape, D. R. Farley, M. W. Bowers, K. G. Krauter, D. H. Munro, O. S. Jones, J. L. Milovich, D. Clark, B. K. Spears, R. P. J. Town, S. W. Haan, S. Dixit, M. B. Schneider, E. L. Dewald, K. Widmann, J. D. Moody, T. Döppner, H. B. Radousky, A. Nikroo, J. J. Kroll, A. V. Hamza, J. B. Horner, S. D. Bhandarkar, E. Dzenitis, E. Alger, E. Giraldez, C. Castro, K. Moreno, C. Haynam, K. N. Lafortune, C. Widmayer, M. Shaw, K. Jancaitis, T. Parham, D. M. Holunga, C. F. Walters, B. Haid, T. Malsbury, D. Trummer, K. R. Coffee, B. Burr, L. V. Berzins, C. Choate, S. J. Brereton, S. Azevedo, H. Chandrasekaran, S. Glenzer, J. A. Caggiano, J. P. Knauer, J. A. Frenje, D. T. Casey, M. G. Johnson, F. H. Séguin, B. K. Young, M. J. Edwards, B. M. Van Wonterghem, J. Kilkenny, B. J. Macgowan, L. J. Atherton, J. D. Lindl, D. D. Meyerhofer and E. Moses, EPJ Web of Conferences **59** (2013).

20. V. A. Smalyuk, L. J. Atherton, L. R. Benedetti, R. Bionta, D. Bleuel, E. Bond, D. K. Bradley, J. Caggiano, D. A. Callahan, D. T. Casey, P. M. Celliers, C. J. Cerjan, D. Clark, E. L. Dewald, S. N. Dixit, T. Doppner, D. H. Edgell, M. J. Edwards, J. Frenje, M. Gatu-Johnson, V. Y. Glebov, S. Glenn, S. H. Glenzer, G. Grim, S. W. Haan, B. A. Hammel, E. P. Hartouni, R. Hatarik, S. Hatchett, D. G. Hicks, W. W. Hsing, N. Izumi, O. S. Jones, M. H. Key, S. F. Khan, J. D. Kilkenny, J. L. Kline, J. Knauer, G. A. Kyrala, O. L. Landen, S. Le Pape, J. D. Lindl, T. Ma, B. J. MacGowan, A. J. Mackinnon, A. G. MacPhee, J. McNaney, N. B. Meezan, J. D. Moody, A. Moore, M. Moran, E. I. Moses, A. Pak, T. Parham, H. S. Park, P. K. Patel, R. Petrasso, J. E. Ralph, S. P. Regan, B. A. Remington, H. F. Robey, J. S. Ross, B. K. Spears, P. T. Springer, L. J. Suter, R. Tommasini, R. P. Town, S. V. Weber and K. Widmann, Phys Rev Lett **111** (21), 215001 (2013).

21. O. L. Landen, R. Benedetti, D. Bleuel, T. R. Boehly, D. K. Bradley, J. A. Caggiano, D. A. Callahan, P. M. Celliers, C. J. Cerjan, D. Clark, G. W. Collins, E. L. Dewald, S. N. Dixit, T.

Doeppner, D. Edgell, J. Eggert, D. Farley, J. A. Frenje, V. Glebov, S. M. Glenn, S. H. Glenzer, S. W. Haan, A. Hamza, B. A. Hammel, C. A. Haynam, J. H. Hammer, R. F. Heeter, H. W. Herrmann, D. G. Hicks, D. E. Hinkel, N. Izumi, M. Gatu Johnson, O. S. Jones, D. H. Kalantar, R. L. Kauffman, J. D. Kilkenny, J. L. Kline, J. P. Knauer, J. A. Koch, G. A. Kyrala, K. LaFortune, T. Ma, A. J. Mackinnon, A. J. Macphee, E. Mapoles, J. L. Milovich, J. D. Moody, N. B. Meezan, P. Michel, A. S. Moore, D. H. Munro, A. Nikroo, R. E. Olson, K. Opachich, A. Pak, T. Parham, P. Patel, H. S. Park, R. P. Petrasso, J. Ralph, S. P. Regan, B. A. Remington, H. G. Rinderknecht, H. F. Robey, M. D. Rosen, J. S. Ross, J. D. Salmonson, T. C. Sangster, M. B. Schneider, V. Smalyuk, B. K. Spears, P. T. Springer, L. J. Suter, C. A. Thomas, R. P. J. Town, S. V. Weber, P. J. Wegner, D. C. Wilson, K. Widmann, C. Yeamans, A. Zylstra, M. J. Edwards, J. D. Lindl, L. J. Atherton, W. W. Hsing, B. J. MacGowan, B. M. Van Wonterghem and E. I. Moses, Plasma Physics and Controlled Fusion **54** (12), 124026 (2012).

22. O. L. Landen, D. T. Casey, J. M. DiNicola, T. Doeppner, E. P. Hartouni, D. E. Hinkel, L. F. Berzak Hopkins, M. Hohenberger, A. L. Kritcher, S. LePape, B. J. MacGowan, S. Maclaren, K. D. Meaney, M. Millot, P. K. Patel, J. Park, L. A. Pickworth, H. F. Robey, J. S. Ross, S. T. Yang, A. B. Zylstra, K. L. Baker, D. A. Callahan, P. M. Celliers, M. J. Edwards, O. A. Hurricane, J. D. Lindl, J. D. Moody, J. Ralph, V. A. Smalyuk, C. A. Thomas, B. M. Van Wonterghem and C. R. Weber, High Energy Density Physics **36**, 100765 (2020).

23. O. A. Hurricane, A. Kritcher, D. A. Callahan, O. Landen, P. K. Patel, P. T. Springer, D. T. Casey, E. L. Dewald, T. R. Dittrich, T. Döppner, D. E. Hinkel, L. F. Berzak Hopkins, J. Kline, S. Le Pape, T. Ma, A. G. MacPhee, A. Moore, A. Pak, H. S. Park, J. Ralph, J. D. Salmonson and K. Widmann, Physics of Plasmas **24** (9), 092706 (2017).

24. H. Abu-Shawareb, R. Acree, P. Adams, J. Adams, B. Addis, R. Aden, P. Adrian, B. B. Afeyan, M. Aggleton, L. Aghaian, A. Aguirre, D. Aikens, J. Akre, F. Albert, M. Albrecht, B. J. Albright, J. Albritton, J. Alcala, C. Alday, D. A. Alessi, N. Alexander, J. Alfonso, N. Alfonso, E. Alger, S. J. Ali, Z. A. Ali, W. E. Alley, P. Amala, P. A. Amendt, P. Amick, S. Ammula, C. Amorin, D. J. Ampleford, R. W. Anderson, T. Anklam, N. Antipa, B. Appelbe, C. Aracne-Ruddle, E. Araya, M. Arend, P. Arnold, T. Arnold, J. Asay, L. J. Atherton, D. Atkinson, R. Atkinson, J. M. Auerbach, B. Austin, L. Auyang, A. S. Awwal, J. Ayers, S. Ayers, T. Ayers, S. Azevedo, B. Bachmann, C. A. Back, J. Bae, D. S. Bailey, J. Bailey, T. Baisden, K. L. Baker, H. Baldis, D. Barber, M. Barberis, D. Barker, A. Barnes, C. W. Barnes, M. A. Barrios, C. Barty, I. Bass, S. H. Batha, S. H. Baxamusa, G. Bazan, J. K. Beagle, R. Beale, B. R. Beck, J. B. Beck, M. Bedzyk, R. G. Beeler, R. G. Beeler, W. Behrendt, L. Belk, P. Bell, M. Belyaev, J. F. Benage, G. Bennett, L. R. Benedetti, L. X. Benedict, R. Berger, T. Bernat, L. A. Bernstein, B. Berry, L. Bertolini, G. Besenbruch, J. Betcher, R. Bettenhausen, R. Betti, B. Bezzerides, S. D. Bhandarkar, R. Bickel, J. Biener, T. Biesiada, K. Bigelow, J. Bigelow-Granillo, V. Bigman, R. M. Bionta, N. W. Birge, M. Bitter, A. C. Black, R. Bleile, D. L. Bleuel, E. Bliss, E. Bliss, B. Blue, T. Boehly, K. Boehm, C. D. Boley, R. Bonanno, E. J. Bond, T. Bond, M. J. Bonino, M. Borden, J. L. Bourgade, J. Bousquet, J. Bowers, M. Bowers, R. Boyd, A. Bozek, D. K. Bradley, K. S. Bradley, P. A. Bradley, L. Bradley, L. Brannon, P. S. Brantley, D. Braun, T. Braun, K. Brienza-Larsen, T. M. Briggs, J. Britten, E. D. Brooks, D. Browning, M. W. Bruhn, T. A. Brunner, H. Bruns, G. Brunton, B. Bryant, T. Buczek, J. Bude, L. Buitano, S. Burkhart, J. Burmark, A. Burnham, R. Burr, L. E. Busby, B. Butlin, R. Cabeltis, M. Cable, W. H. Cabot, B. Cagadas, J. Caggiano, R. Cahayag, S. E. Caldwell, S. Calkins, D. A. Callahan, J. Calleja-Aguirre, L. Camara, D. Camp, E. M. Campbell, J. H. Campbell, B. Carey, R. Carey, K. Carlisle, L. Carlson, L. Carman, J. Carmichael, A. Carpenter, C. Carr, J. A. Carrera, D.

Casavant, A. Casey, D. T. Casey, A. Castillo, E. Castillo, J. I. Castor, C. Castro, W. Caughey, R. Cavitt, J. Celeste, P. M. Celliers, C. Cerjan, G. Chandler, B. Chang, C. Chang, J. Chang, L. Chang, R. Chapman, T. Chapman, L. Chase, H. Chen, H. Chen, K. Chen, L. Y. Chen, B. Cheng, J. Chittenden, C. Choate, J. Chou, R. E. Chrien, M. Chrisp, K. Christensen, M. Christensen, A. R. Christopherson, M. Chung, J. A. Church, A. Clark, D. S. Clark, K. Clark, R. Clark, L. Claus, B. Cline, J. A. Cline, J. A. Cobble, K. Cochrane, B. Cohen, S. Cohen, M. R. Collette, G. Collins, L. A. Collins, T. J. B. Collins, A. Conder, B. Conrad, M. Conyers, A. W. Cook, D. Cook, R. Cook, J. C. Cooley, G. Cooper, T. Cope, S. R. Copeland, F. Coppari, J. Cortez, J. Cox, D. H. Crandall, J. Crane, R. S. Craxton, M. Cray, A. Crilly, J. W. Crippen, D. Cross, M. Cuneo, G. Cuotts, C. E. Czajka, D. Czechowicz, T. Daly, P. Danforth, R. Darbee, B. Darlington, P. Datte, L. Dauffy, G. Davalos, S. Davidovits, P. Davis, J. Davis, S. Dawson, R. D. Day, T. H. Day, M. Dayton, C. Deck, C. Decker, C. Deeney, K. A. DeFriend, G. Deis, N. D. Delamater, J. A. Delettrez, R. Demaret, S. Demos, S. M. Dempsey, R. Desjardin, T. Desjardins, M. P. Desjarlais, E. L. Dewald, J. DeYoreo, S. Diaz, G. Dimonte, T. R. Dittrich, L. Divol, S. N. Dixit, J. Dixon, E. S. Dodd, D. Dolan, A. Donovan, M. Donovan, T. Doppner, C. Dorrer, N. Dorsano, M. R. Douglas, D. Dow, J. Downie, E. Downing, M. Dozieres, V. Draggoo, D. Drake, R. P. Drake, T. Drake, G. Dreifuerst, D. F. DuBois, P. F. DuBois, G. Dunham, R. Dylla-Spears, A. K. L. Dymoke-Bradshaw, B. Dzenitis, C. Ebbers, M. Eckart, S. Eddinger, D. Eder, D. Edgell, M. J. Edwards, P. Efthimion, J. H. Eggert, B. Ehrlich, P. Ehrmann, S. Elhadj, C. Ellerbee, N. S. Elliott, C. L. Ellison, F. Elsner, M. Emerich, K. Engelhorn, T. England, E. English, P. Epperson, R. Epstein, G. Erbert, M. A. Erickson, D. J. Erskine, A. Erlandson, R. J. Espinosa, C. Estes, K. G. Estabrook, S. Evans, A. Fabyan, J. Fair, R. Fallejo, N. Farmer, W. A. Farmer, M. Farrell, V. E. Fatherley, M. Fedorov, E. Feigenbaum, M. Feit, W. Ferguson, J. C. Fernandez, A. Fernandez-Panella, S. Fess, J. E. Field, C. V. Filip, J. R.

Fincke, T. Finn, S. M. Finnegan, R. G. Finucane, M. Fischer, A. Fisher, J. Fisher, B. Fishler, D. Fittinghoff, P. Fitzsimmons, M. Flegel, K. A. Flippo, J. Florio, J. Folta, P. Folta, L. R. Foreman, C. Forrest, A. Forsman, J. Fooks, M. Foord, R. Fortner, K. Fournier, D. E. Fratanduono, N. Frazier, T. Frazier, C. Frederick, M. S. Freeman, J. Frenje, D. Frey, G. Frieders, S. Friedrich, D. H. Froula, J. Fry, T. Fuller, J. Gaffney, S. Gales, B. Le Galloudec, K. K. Le Galloudec, A. Gambhir, L. Gao, W. J. Garbett, A. Garcia, C. Gates, E. Gaut, P. Gauthier, Z. Gavin, J. Gaylord, M. Geissel, F. Genin, J. Georgeson, H. Geppert-Kleinrath, V. Geppert-Kleinrath, N. Gharibyan, J. Gibson, C. Gibson, E. Giraldez, V. Glebov, S. G. Glendinning, S. Glenn, S. H. Glenzer, S. Goade, P. L. Gobby, S. R. Goldman, B. Golick, M. Gomez, V. Goncharov, D. Goodin, P. Grabowski, E. Grafil, P. Graham, J. Grandy, E. Grasz, F. Graziani, G. Greenman, J. A. Greenough, A. Greenwood, G. Gregori, T. Green, J. R. Griego, G. P. Grim, J. Grondalski, S. Gross, J. Guckian, N. Guler, B. Gunney, G. Guss, S. Haan, J. Hackbarth, L. Hackel, R. Hackel, C. Haefner, C. Hagmann, K. D. Hahn, S. Hahn, B. J. Haid, B. M. Haines, B. M. Hall, C. Hall, G. N. Hall, M. Hamamoto, S. Hamel, C. E. Hamilton, B. A. Hammel, J. H. Hammer, G. Hampton, A. Hamza, A. Handler, S. Hansen, D. Hanson, R. Haque, D. Harding, E. Harding, J. D. Hares, D. B. Harris, J. A. Harte, E. P. Hartouni, R. Hatarik, S. Hatchett, A. A. Hauer, M. Havre, R. Hawley, J. Hayes, J. Hayes, S. Hayes, A. Hayes-Sterbenz, C. A. Haynam, D. A. Haynes, D. Headley, A. Heal, J. E. Heebner, S. Heerey, G. M. Heestand, R. Heeter, N. Hein, C. Heinbockel, C. Hendricks, M. Henesian, J. Heninger, J. Henrikson, E. A. Henry, E. B. Herbold, M. R. Hermann, G. Hermes, J. E. Hernandez, V. J. Hernandez, M. C. Herrmann, H. W. Herrmann, O. D. Herrera, D. Hewett, R. Hibbard, D. G. Hicks, D. Hill, K. Hill, T. Hilsabeck, D. E. Hinkel, D. D. Ho, V. K. Ho, J. K. Hoffer, N. M. Hoffman, M. Hohenberger, M. Hohensee, W. Hoke, D. Holdener, F. Holdener, J. P. Holder, B. Holko, D. Holunga, J. F. Holzrichter, J. Honig, D. Hoover, D. Hopkins, L. Berzak Hopkins, M. Hoppe, M.

L. Hoppe, J. Horner, R. Hornung, C. J. Horsfield, J. Horvath, D. Hotaling, R. House, L. Howell, W. W. Hsing, S. X. Hu, H. Huang, J. Huckins, H. Hui, K. D. Humbird, J. Hund, J. Hunt, O. A. Hurricane, M. Hutton, K. H. Huynh, L. Inandan, C. Iglesias, I. V. Igumenshchev, N. Izumi, M. Jackson, J. Jackson, S. D. Jacobs, G. James, K. Jancaitis, J. Jarboe, L. C. Jarrott, D. Jasion, J. Jaquez, J. Jeet, A. E. Jenei, J. Jensen, J. Jimenez, R. Jimenez, D. Jobe, Z. Johal, H. M. Johns, D. Johnson, M. A. Johnson, M. Gatu Johnson, R. J. Johnson, S. Johnson, S. A. Johnson, T. Johnson, K. Jones, O. Jones, M. Jones, R. Jorge, H. J. Jorgenson, M. Julian, B. I. Jun, R. Jungquist, J. Kaae, N. Kabadi, D. Kaczala, D. Kalantar, K. Kangas, V. V. Karasiev, M. Karasik, V. Karpenko, A. Kasarky, K. Kasper, R. Kauffman, M. I. Kaufman, C. Keane, L. Keaty, L. Kegelmeyer, P. A. Keiter, P. A. Kellett, J. Kellogg, J. H. Kelly, S. Kemic, A. J. Kemp, G. E. Kemp, G. D. Kerbel, D. Kershaw, S. M. Kerr, T. J. Kessler, M. H. Key, S. F. Khan, H. Khater, C. Kiikka, J. Kilkenny, Y. Kim, Y. J. Kim, J. Kimko, M. Kimmel, J. M. Kindel, J. King, R. K. Kirkwood, L. Klaus, D. Klem, J. L. Kline, J. Klingmann, G. Kluth, P. Knapp, J. Knauer, J. Knipping, M. Knudson, D. Kobs, J. Koch, T. Kohut, C. Kong, J. M. Koning, P. Koning, S. Konior, H. Kornblum, L. B. Kot, B. Kozioziemski, M. Kozlowski, P. M. Kozlowski, J. Krammen, N. S. Krasheninnikova, B. Kraus, W. Krauser, J. D. Kress, A. L. Kritcher, E. Krieger, J. J. Kroll, W. L. Kruer, M. K. G. Kruse, S. Kucheyev, M. Kumbera, S. Kumpan, J. Kunimune, B. Kustowski, T. J. T. Kwan, G. A. Kyrala, S. Laffite, M. Lafon, K. LaFortune, B. Lahmann, B. Lairson, O. L. Landen, J. Langenbrunner, L. Lagin, T. Land, M. Lane, D. Laney, A. B. Langdon, S. H. Langer, A. Langro, N. E. Lanier, T. E. Lanier, D. Larson, B. F. Lasinski, D. Lassle, D. LaTray, G. Lau, N. Lau, C. Laumann, A. Laurence, T. A. Laurence, J. Lawson, H. P. Le, R. R. Leach, L. Leal, A. Leatherland, K. LeChien, B. Lechleiter, A. Lee, M. Lee, T. Lee, R. J. Leeper, E. Lefebvre, J. P. Leidinger, B. LeMire, R. W. Lemke, N. C. Lemos, S. Le Pape, R. Lerche, S. Lerner, S. Letts, K. Levedahl, T. Lewis, C. K. Li,

H. Li, J. Li, W. Liao, Z. M. Liao, D. Liedahl, J. Liebman, G. Lindford, E. L. Lindman, J. D. Lindl, H. Loey, R. A. London, F. Long, E. N. Loomis, F. E. Lopez, H. Lopez, E. Losbanos, S. Loucks, R. Lowe-Webb, E. Lundgren, A. P. Ludwigsen, R. Luo, J. Lusk, R. Lyons, T. Ma, Y. Macallop, M. J. MacDonald, B. J. MacGowan, J. M. Mack, A. J. Mackinnon, S. A. MacLaren, A. G. MacPhee, G. R. Magelssen, J. Magoon, R. M. Malone, T. Malsbury, R. Managan, R. Mancini, K. Manes, D. Maney, D. Manha, O. M. Mannion, A. M. Manuel, E. Mapoles, G. Mara, T. Marcotte, E. Marin, M. M. Marinak, C. Mariscal, D. A. Mariscal, E. F. Mariscal, E. V. Marley, J. A. Marozas, R. Marquez, C. D. Marshall, F. J. Marshall, M. Marshall, S. Marshall, J. Marticorena, D. Martinez, I. Maslennikov, D. Mason, R. J. Mason, L. Masse, W. Massey, P. E. Masson-Laborde, N. D. Masters, D. Mathisen, E. Mathison, J. Matone, M. J. Matthews, C. Mattoon, T. R. Mattsson, K. Matzen, C. W. Mauche, M. Mauldin, T. McAbee, M. McBurney, T. McCarville, R. L. McCrory, A. M. McEvoy, C. McGuffey, M. McInnis, P. McKenty, M. S. McKinley, J. B. McLeod, A. McPherson, B. McQuillan, M. Meamber, K. D. Meaney, N. B. Meezan, R. Meissner, T. A. Mehlhorn, N. C. Mehta, J. Menapace, F. E. Merrill, B. T. Merritt, E. C. Merritt, D. D. Meyerhofer, S. Mezyk, R. J. Mich, P. A. Michel, D. Milam, C. Miller, D. Miller, D. S. Miller, E. Miller, E. K. Miller, J. Miller, M. Miller, P. E. Miller, T. Miller, W. Miller, V. Miller-Kamm, M. Millot, J. L. Milovich, P. Minner, J. L. Miquel, S. Mitchell, K. Molvig, R. C. Montesanti, D. S. Montgomery, M. Monticelli, A. Montoya, J. D. Moody, A. S. Moore, E. Moore, M. Moran, J. C. Moreno, K. Moreno, B. E. Morgan, T. Morrow, J. W. Morton, E. Moses, K. Moy, R. Muir, M. S. Murillo, J. E. Murray, J. R. Murray, D. H. Munro, T. J. Murphy, F. M. Munteanu, J. Nafziger, T. Nagayama, S. R. Nagel, R. Nast, R. A. Negres, A. Nelson, D. Nelson, J. Nelson, S. Nelson, S. Nemethy, P. Neumayer, K. Newman, M. Newton, H. Nguyen, J. G. Di Nicola, P. Di Nicola, C. Niemann, A. Nikroo, P. M. Nilson, A. Nobile, V. Noorai, R. Nora, M. Norton, M. Nostrand, V. Note, S. Novell,

P. F. Nowak, A. Nunez, R. A. Nyholm, M. O'Brien, A. Oceguera, J. A. Oertel, J. Okui, B. Olejniczak, J. Oliveira, P. Olsen, B. Olson, K. Olson, R. E. Olson, Y. P. Opachich, N. Orsi, C. D. Orth, M. Owen, S. Padalino, E. Padilla, R. Paguio, S. Paguio, J. Paisner, S. Pajoom, A. Pak, S. Palaniyappan, K. Palma, T. Pannell, F. Papp, D. Paras, T. Parham, H. S. Park, A. Pasternak, S. Patankar, M. V. Patel, P. K. Patel, R. Patterson, S. Patterson, B. Paul, M. Paul, E. Pauli, O. T. Pearce, J. Pearcy, B. Pedrotti, A. Peer, L. J. Pelz, B. Penetrante, J. Penner, A. Perez, L. J. Perkins, E. Pernice, T. S. Perry, S. Person, D. Petersen, T. Petersen, D. L. Peterson, E. B. Peterson, J. E. Peterson, J. L. Peterson, K. Peterson, R. R. Peterson, R. D. Petrasso, F. Philippe, T. J. Phipps, E. Piceno, Y. Ping, L. Pickworth, J. Pino, R. Plummer, G. D. Pollack, S. M. Pollaine, B. B. Pollock, D. Ponce, J. Ponce, J. Pontelandolfo, J. L. Porter, J. Post, O. Poujade, C. Powell, H. Powell, G. Power, M. Pozulp, M. Prantil, M. Prasad, S. Pratuch, S. Price, K. Primdahl, S. Prisbrey, R. Procassini, A. Pruyne, B. Pudliner, S. R. Qiu, K. Quan, M. Quinn, J. Quintenz, P. B. Radha, F. Rainer, J. E. Ralph, K. S. Raman, R. Raman, P. Rambo, S. Rana, A. Randewich, D. Rardin, M. Ratledge, N. Ravelo, F. Ravizza, M. Rayce, A. Raymond, B. Raymond, B. Reed, C. Reed, S. Regan, B. Reichelt, V. Reis, S. Reisdorf, V. Rekow, B. A. Remington, A. Rendon, W. Requieron, M. Rever, H. Reynolds, J. Reynolds, J. Rhodes, M. Rhodes, M. C. Richardson, B. Rice, N. G. Rice, R. Rieben, A. Rigatti, S. Riggs, H. G. Rinderknecht, K. Ring, B. Riordan, R. Riquier, C. Rivers, D. Roberts, V. Roberts, G. Robertson, H. F. Robey, J. Robles, P. Rocha, G. Rochau, J. Rodriguez, S. Rodriguez, M. Rosen, M. Rosenberg, G. Ross, J. S. Ross, P. Ross, J. Rouse, D. Rovang, A. M. Rubenchik, M. S. Rubery, C. L. Ruiz, M. Rushford, B. Russ, J. R. Rygg, B. S. Ryujin, R. A. Sacks, R. F. Sacks, K. Saito, T. Salmon, J. D. Salmonson, J. Sanchez, S. Samuelson, M. Sanchez, C. Sangster, A. Saroyan, J. Sater, A. Satsangi, S. Sauers, R. Saunders, J. P. Sauppe, R. Sawicki, D. Sayre, M. Scanlan, K. Schaffers, G. T. Schappert, S. Schiaffino, D. J. Schlossberg,

D. W. Schmidt, M. J. Schmitt, D. H. G. Schneider, M. B. Schneider, R. Schneider, M. Schoff, M. Schollmeier, M. Scholmerich, C. R. Schroeder, S. E. Schrauth, H. A. Scott, I. Scott, J. M. Scott, R. H. H. Scott, C. R. Scullard, T. Sedillo, F. H. Seguin, W. Seka, J. Senecal, S. M. Sepke, L. Seppala, K. Sequoia, J. Severyn, J. M. Sevier, N. Sewell, S. Seznec, R. C. Shah, J. Shamlian, D. Shaughnessy, M. Shaw, R. Shaw, C. Shearer, R. Shelton, N. Shen, M. W. Sherlock, A. I. Shestakov, E. L. Shi, S. J. Shin, N. Shingleton, W. Shmayda, M. Shor, M. Shoup, C. Shuldberg, L. Siegel, F. J. Silva, A. N. Simakov, B. T. Sims, D. Sinars, P. Singh, H. Sio, K. Skulina, S. Skupsky, S. Slutz, M. Sluyter, V. A. Smalyuk, D. Smauley, R. M. Smeltser, C. Smith, I. Smith, J. Smith, L. Smith, R. Smith, R. Sohn, S. Sommer, C. Sorce, M. Sorem, J. M. Soures, M. L. Spaeth, B. K. Spears, S. Speas, D. Speck, R. Speck, J. Spears, T. Spinka, P. T. Springer, M. Stadermann, B. Stahl, J. Stahoviak, L. G. Stanton, R. Steele, W. Steele, D. Steinman, R. Stemke, R. Stephens, S. Sterbenz, P. Sterne, D. Stevens, J. Stevers, C. B. Still, C. Stoeckl, W. Stoeffl, J. S. Stolken, C. Stolz, E. Storm, G. Stone, S. Stoupin, E. Stout, I. Stowers, R. Strauser, H. Streckart, J. Streit, D. J. Strozzi, T. Suratwala, G. Sutcliffe, L. J. Suter, S. B. Sutton, V. Svidzinski, G. Swadling, W. Sweet, A. Szoke, M. Tabak, M. Takagi, A. Tambazidis, V. Tang, M. Taranowski, L. A. Taylor, S. Telford, W. Theobald, M. Thi, A. Thomas, C. A. Thomas, I. Thomas, R. Thomas, I. J. Thompson, A. Thongstisubskul, C. B. Thorsness, G. Tietbohl, R. E. Tipton, M. Tobin, N. Tomlin, R. Tommasini, A. J. Toreja, J. Torres, R. P. J. Town, S. Townsend, J. Trenholme, A. Trivelpiece, C. Trosseille, H. Truax, D. Trummer, S. Trummer, T. Truong, D. Tubbs, E. R. Tubman, T. Tunnell, D. Turnbull, R. E. Turner, M. Ulitsky, R. Upadhye, J. L. Vaher, P. VanArsdall, D. VanBlarcom, M. Vandenboomgaerde, R. VanQuinlan, B. M. Van Wonterghem, W. S. Varnum, A. L. Velikovich, A. Vella, C. P. Verdon, B. Vermillion, S. Vernon, R. Vesey, J. Vickers, R. M. Vignes, M. Visosky, J. Vocke, P. L. Volegov, S. Vonhof, R. Von Rotz, H. X. Vu, M. Vu, D. Wall, J. Wall, R. Wallace,

B. Wallin, D. Walmer, C. A. Walsh, C. F. Walters, C. Waltz, A. Wan, A. Wang, Y. Wang, J. S. Wark, B. E. Warner, J. Watson, R. G. Watt, P. Watts, J. Weaver, R. P. Weaver, S. Weaver, C. R. Weber, P. Weber, S. V. Weber, P. Wegner, B. Welday, L. Welser-Sherrill, K. Weiss, K. Widmann, G. F. Wheeler, W. Whistler, R. K. White, H. D. Whitley, P. Whitman, M. E. Wickett, C. Widmayer, J. Wiedwald, R. Wilcox, S. Wilcox, C. Wild, B. H. Wilde, C. H. Wilde, K. Wilhelmsen, M. D. Wilke, H. Wilkens, P. Wilkins, S. C. Wilks, E. A. Williams, G. J. Williams, W. Williams, W. H. Williams, D. C. Wilson, B. Wilson, E. Wilson, R. Wilson, S. Winters, J. Wisoff, M. Wittman, J. Wolfe, A. Wong, K. W. Wong, L. Wong, N. Wong, R. Wood, D. Woodhouse, J. Woodruff, D. T. Woods, S. Woods, B. N. Woodworth, E. Wooten, A. Wootton, K. Work, J. B. Workman, J. Wright, M. Wu, C. Wuest, F. J. Wysocki, H. Xu, M. Yamaguchi, B. Yang, S. T. Yang, J. Yatabe, C. B. Yeamans, B. C. Yee, S. A. Yi, L. Yin, B. Young, C. S. Young, C. V. Young, P. Young, K. Youngblood, R. Zacharias, G. Zagaris, N. Zaitseva, F. Zaka, F. Ze, B. Zeiger, M. Zika, G. B. Zimmerman, T. Zobrist, J. D. Zuegel, A. B. Zylstra and I. C. F. C. Indirect Drive, Phys Rev Lett **129** (7), 075001 (2022).

25. J. D. Moody, O. L. Landen, L. Divol, S. LePape, P. Michel, R. P. J. Town, G. Hall, K. Widmann and A. Moore, Physics of Plasmas **24** (4) (2017).

26. J. D. Lindl, P. Amendt, R. L. Berger, S. G. Glendinning, S. H. Glenzer, S. W. Haan, R. L. Kauffman, O. L. Landen and L. J. Suter, Physics of Plasmas **11** (2), 339-491 (2004).

27. J. Schein, O. Jones, M. Rosen, E. Dewald, S. Glenzer, J. Gunther, B. Hammel, O. Landen, L. Suter and R. Wallace, Physical Review Letters **98** (2007).

28. K. Baker, C. Thomas, O. Landen, S. Haan, J. Lindl, D. Casey, C. Young, R. Nora, O. Hurricane, D. Callahan, O. Jones, L. Berzak Hopkins, S. Khan, B. Spears, S. Le Pape, N. Meezan, D. Ho, T. Döppner, D. Hinkel, E. Dewald, R. Tommasini, M. Hohenberger, C. Weber, D. Clark,

D. Woods, J. Milovich, D. Strozzi, A. Kritcher, H. Robey, J. Ross, V. Smalyuk, P. Amendt, B. Bachmann, L. Benedetti, R. Bionta, P. Celliers, D. Fittinghoff, C. Goyon, R. Hatarik, N. Izumi, M. Gatu Johnson, G. Kyrala, T. Ma, K. Meaney, M. Millot, S. Nagel, P. Patel, D. Turnbull, P. Volegov, C. Yeamans and B. H. Wilde, Physics of Plasmas **30** (3), 032702 (2023).

29. K. L. Baker, C. A. Thomas, D. T. Casey, S. Khan, B. K. Spears, R. Nora, T. Woods, J. L. Milovich, R. L. Berger, D. Strozzi, D. Clark, M. Hohenberger, O. A. Hurricane, D. A. Callahan, O. L. Landen, B. Bachmann, R. Benedetti, R. Bionta, P. M. Celliers, D. Fittinghoff, C. Goyon, G. Grim, R. Hatarik, N. Izumi, M. Gatu Johnson, G. Kyrala, T. Ma, M. Millot, S. R. Nagel, A. Pak, P. K. Patel, D. Turnbull, P. L. Volegov and C. Yeamans, Phys Rev Lett **121** (13), 135001 (2018).

30. K. L. Baker, (LLNL, 2019).

31. K. L. Baker, O. Jones, C. Weber, D. Clark, P. K. Patel, C. A. Thomas, O. L. Landen, R. Nora, G. J. Anderson, J. Gaffney, S. MacLaren, D. T. Casey, T. Döppner, E. L. Dewald, R. Tommasini, B. K. Spears, J. Salmonson, M. Hohenberger, S. Khan, A. Zylstra, A. Kritcher, P. Amendt, V. Smalyuk, J. Lindl, C. Young, J. S. Ross, D. Ho, O. A. Hurricane, D. A. Callahan, T. Woods, J. L. Milovich, D. J. Strozzi, B. Bachmann, R. Bionta, P. M. Celliers, D. Fittinghoff, R. Hatarik, M. Gatu Johnson, K. Meaney, M. Millot, P. L. Volegov and C. Wilde, Physics of Plasmas **29** (6), 062705 (2022).

32. K. L. Baker, S. MacLaren, O. Jones, B. K. Spears, P. K. Patel, R. Nora, L. Divol, O. L. Landen, G. J. Anderson, J. Gaffney, M. Kruse, O. A. Hurricane, D. A. Callahan, A. R. Christopherson, J. Salmonson, E. P. Hartouni, T. Döppner, E. Dewald, R. Tommasini, C. A. Thomas, C. Weber, D. Clark, D. T. Casey, M. Hohenberger, S. Khan, T. Woods, J. L. Milovich, R. L. Berger, D. Strozzi, A. Kritcher, B. Bachmann, R. Benedetti, R. Bionta, P. M. Celliers, D. Fittinghoff, R. Hatarik, N. Izumi, M. Gatu Johnson, G. Kyrala, T. Ma, K. Meaney, M. Millot, S.

R. Nagel, A. Pak, P. L. Volegov, C. Yeamans and C. Wilde, Physical Review E **107** (1), 015202 (2023).

33. K. L. Baker, C. A. Thomas, D. T. Casey, M. Hohenberger, S. Khan, B. K. Spears, O. L. Landen, R. Nora, D. T. Woods, J. L. Milovich, R. L. Berger, D. Strozzi, C. Weber, D. Clark, O. A. Hurricane, D. A. Callahan, A. L. Kritcher, B. Bachmann, L. R. Benedetti, R. Bionta, P. M. Celliers, D. Fittinghoff, C. Goyon, R. Hatarik, N. Izumi, M. Gatu Johnson, G. Kyrala, T. Ma, K. Meaney, M. Millot, S. R. Nagel, P. K. Patel, D. Turnbull, P. L. Volegov, C. Yeamans and C. Wilde, Phys Rev E **102** (2-1), 023210 (2020).

34. P. K. Patel, P. T. Springer, C. R. Weber, L. C. Jarrott, O. A. Hurricane, B. Bachmann, K. L. Baker, L. F. Berzak Hopkins, D. A. Callahan, D. T. Casey, C. J. Cerjan, D. S. Clark, E. L. Dewald, L. Divol, T. Döppner, J. E. Field, D. Fittinghoff, J. Gaffney, V. Geppert-Kleinrath, G. P. Grim, E. P. Hartouni, R. Hatarik, D. E. Hinkel, M. Hohenberger, K. Humbird, N. Izumi, O. S. Jones, S. F. Khan, A. L. Kritcher, M. Kruse, O. L. Landen, S. Le Pape, T. Ma, S. A. MacLaren, A. G. MacPhee, L. P. Masse, N. B. Meezan, J. L. Milovich, R. Nora, A. Pak, J. L. Peterson, J. Ralph, H. F. Robey, J. D. Salmonson, V. A. Smalyuk, B. K. Spears, C. A. Thomas, P. L. Volegov, A. Zylstra and M. J. Edwards, Physics of Plasmas **27** (5) (2020).

35. D. T. Casey, C. A. Thomas, K. L. Baker, B. K. Spears, M. Hohenberger, S. F. Khan, R. C. Nora, C. R. Weber, D. T. Woods, O. A. Hurricane, D. A. Callahan, R. L. Berger, J. L. Milovich, P. K. Patel, T. Ma, A. Pak, L. R. Benedetti, M. Millot, C. Jarrott, O. L. Landen, R. M. Bionta, B. J. MacGowan, D. J. Strozzi, M. Stadermann, J. Biener, A. Nikroo, C. S. Goyon, N. Izumi, S. R. Nagel, B. Bachmann, P. L. Volegov, D. N. Fittinghoff, G. P. Grim, C. B. Yeamans, M. Gatu Johnson, J. A. Frenje, N. Rice, C. Kong, J. Crippen, J. Jaquez, K. Kangas and C. Wild, Physics of Plasmas **25** (5) (2018).

36. C. A. Thomas, E. M. Campbell, K. L. Baker, D. T. Casey, M. Hohenberger, A. L. Kritcher, B. K. Spears, S. F. Khan, R. Nora, D. T. Woods, J. L. Milovich, R. L. Berger, D. Strozzi, D. D. Ho, D. Clark, B. Bachmann, L. R. Benedetti, R. Bionta, P. M. Celliers, D. N. Fittinghoff, G. Grim, R. Hatarik, N. Izumi, G. Kyrala, T. Ma, M. Millot, S. R. Nagel, P. K. Patel, C. Yeamans, A. Nikroo, M. Tabak, M. Gatu Johnson, P. L. Volegov and S. M. Finnegan, Physics of Plasmas **27** (11) (2020).

37. C. A. Thomas, E. M. Campbell, K. L. Baker, D. T. Casey, M. Hohenberger, A. L. Kritcher, B. K. Spears, S. F. Khan, R. Nora, D. T. Woods, J. L. Milovich, R. L. Berger, D. Strozzi, D. D. Ho, D. Clark, B. Bachmann, L. R. Benedetti, R. Bionta, P. M. Celliers, D. N. Fittinghoff, G. Grim, R. Hatarik, N. Izumi, G. Kyrala, T. Ma, M. Millot, S. R. Nagel, P. K. Patel, C. Yeamans, A. Nikroo, M. Tabak, M. Gatu Johnson, P. L. Volegov and S. M. Finnegan, Physics of Plasmas **27**, 112712 (2020).

38. C. A. Thomas, E. M. Campbell, K. L. Baker, D. T. Casey, M. Hohenberger, A. L. Kritcher, B. K. Spears, S. F. Khan, R. Nora, D. T. Woods, J. L. Milovich, R. L. Berger, D. Strozzi, D. D. Ho, D. Clark, B. Bachmann, L. R. Benedetti, R. Bionta, P. M. Celliers, D. N. Fittinghoff, G. Grim, R. Hatarik, N. Izumi, G. Kyrala, T. Ma, M. Millot, S. R. Nagel, P. K. Patel, C. Yeamans, A. Nikroo, M. Tabak, M. Gatu Johnson, P. L. Volegov and S. M. Finnegan, Physics of Plasmas **27**, 112708 (2020).

39. M. Hohenberger, D. T. Casey, C. A. Thomas, O. L. Landen, K. L. Baker, L. R. Benedetti, D. A. Callahan, O. A. Hurricane, N. Izumi, S. F. Khan, T. Ma, D. A. Mariscal, S. R. Nagel, A. Pak and B. K. Spears, Physics of Plasmas **26** (11) (2019).

40. R. Berger, Thomas, Cliff A., K. Baker, D. Casey, C. Goyon, J. Park, N. Lemos, S. Khan, M. Hohenberger, J. Milovich, D. Strozzi, M. Belyaev, T. Chapman and A. B. Langdon, Physics of Plasmas **26**, 012709 (2019).

41. A. J. MacKinnon, N. B. Meezan, J. S. Ross, S. Le Pape, L. Berzak Hopkins, L. Divol, D. Ho, J. Milovich, A. Pak, J. Ralph, T. Döppner, P. K. Patel, C. Thomas, R. Tommasini, S. Haan, A. G. MacPhee, J. McNaney, J. Caggiano, R. Hatarik, R. Bionta, T. Ma, B. Spears, J. R. Rygg, L. R. Benedetti, R. P. J. Town, D. K. Bradley, E. L. Dewald, D. Fittinghoff, O. S. Jones, H. R. Robey, J. D. Moody, S. Khan, D. A. Callahan, A. Hamza, J. Biener, P. M. Celliers, D. G. Braun, D. J. Erskine, S. T. Prisbrey, R. J. Wallace, B. Kozioziemski, R. Dylla-Spears, J. Sater, G. Collins, E. Storm, W. Hsing, O. Landen, J. L. Atherton, J. D. Lindl, M. J. Edwards, J. A. Frenje, M. Gatu-Johnson, C. K. Li, R. Petrasso, H. Rinderknecht, M. Rosenberg, F. H. Séguin, A. Zylstra, J. P. Knauer, G. Grim, N. Guler, F. Merrill, R. Olson, G. A. Kyrala, J. D. Kilkenny, A. Nikroo, K. Moreno, D. E. Hoover, C. Wild and E. Werner, Physics of Plasmas **21** (5), 056318 (2014).

42. S. Le Pape, L. F. Berzak Hopkins, L. Divol, A. Pak, E. L. Dewald, S. Bhandarkar, L. R. Bennedetti, T. Bunn, J. Biener, J. Crippen, D. Casey, D. Edgell, D. N. Fittinghoff, M. Gatu-Johnson, C. Goyon, S. Haan, R. Hatarik, M. Havre, D. D. Ho, N. Izumi, J. Jaquez, S. F. Khan, G. A. Kyrala, T. Ma, A. J. Mackinnon, A. G. MacPhee, B. J. MacGowan, N. B. Meezan, J. Milovich, M. Millot, P. Michel, S. R. Nagel, A. Nikroo, P. Patel, J. Ralph, J. S. Ross, N. G. Rice, D. Strozzi, M. Stadermann, P. Volegov, C. Yeamans, C. Weber, C. Wild, D. Callahan and O. A. Hurricane, Phys Rev Lett **120** (24), 245003 (2018).

43. L. F. Berzak Hopkins, N. B. Meezan, S. Le Pape, L. Divol, A. J. Mackinnon, D. D. Ho, M. Hohenberger, O. S. Jones, G. Kyrala, J. L. Milovich, A. Pak, J. E. Ralph, J. S. Ross, L. R. Benedetti, J. Biener, R. Bionta, E. Bond, D. Bradley, J. Caggiano, D. Callahan, C. Cerjan, J. Church, D. Clark, T. Doppner, R. Dylla-Spears, M. Eckart, D. Edgell, J. Field, D. N. Fittinghoff, M. Gatu Johnson, G. Grim, N. Guler, S. Haan, A. Hamza, E. P. Hartouni, R. Hatarik, H. W. Herrmann, D. Hinkel, D. Hoover, H. Huang, N. Izumi, S. Khan, B. Kozioziemski, J. Kroll, T. Ma,

A. MacPhee, J. McNaney, F. Merrill, J. Moody, A. Nikroo, P. Patel, H. F. Robey, J. R. Rygg, J. Sater, D. Sayre, M. Schneider, S. Sepke, M. Stadermann, W. Stoeffl, C. Thomas, R. P. Town, P. L. Volegov, C. Wild, C. Wilde, E. Woerner, C. Yeamans, B. Yoxall, J. Kilkenny, O. L. Landen, W. Hsing and M. J. Edwards, Phys Rev Lett **114** (17), 175001 (2015).

44. N. B. Meezan, L. F. Berzak Hopkins, S. Le Pape, L. Divol, A. J. MacKinnon, T. Döppner, D. D. Ho, O. S. Jones, S. F. Khan, T. Ma, J. L. Milovich, A. E. Pak, J. S. Ross, C. A. Thomas, L. R. Benedetti, D. K. Bradley, P. M. Celliers, D. S. Clark, J. E. Field, S. W. Haan, N. Izumi, G. A. Kyrala, J. D. Moody, P. K. Patel, J. E. Ralph, J. R. Rygg, S. M. Sepke, B. K. Spears, R. Tommasini, R. P. J. Town, J. Biener, R. M. Bionta, E. J. Bond, J. A. Caggiano, M. J. Eckart, M. Gatu Johnson, G. P. Grim, A. V. Hamza, E. P. Hartouni, R. Hatarik, D. E. Hoover, J. D. Kilkenny, B. J. Kozioziemski, J. J. Kroll, J. M. McNaney, A. Nikroo, D. B. Sayre, M. Stadermann, C. Wild, B. E. Yoxall, O. L. Landen, W. W. Hsing and M. J. Edwards, Physics of Plasmas **22** (6) (2015).

45. D. D. M. Ho, S. W. Haan, J. D. Salmonson, D. S. Clark, J. D. Lindl, J. L. Milovich, C. A. Thomas, L. F. Berzak Hopkins and N. B. Meezan, Journal of Physics: Conference Series **717** (2016).

46. L. Divol, A. Pak, L. F. Berzak Hopkins, S. L. Pape, N. B. Meezan, E. L. Dewald, D. D. M. Ho, S. F. Khan, A. J. Mackinnon, J. S. Ross, D. P. Turnbull, C. Weber, P. M. Celliers, M. Millot, L. R. Benedetti, J. E. Field, N. Izumi, G. A. Kyrala, T. Ma, S. R. Nagel, J. R. Rygg, D. Edgell, A. G. Macphee, C. Goyon, M. Hohenberger, B. J. MacGowan, P. Michel, D. Strozzi, W. S. Cassata, D. Casey, D. N. Fittinghoff, N. Gharibyan, R. Hatarik, D. Sayre, P. Volegov, C. Yeamans, B. Bachmann, T. Döppner, J. Biener, J. Crippen, C. Choate, H. Huang, C. Kong, A. Nikroo, N. G. Rice, M. Stadermann, S. D. Bhandarkar, S. Haan, B. Kozioziemski, W. W. Hsing, O. L. Landen,

J. D. Moody, R. P. J. Town, D. A. Callahan, O. A. Hurricane and M. J. Edwards, Physics of Plasmas **24** (5), 056309 (2017).

47. A. L. Kritcher, C. Young, H. F. Robey and others, Nature Physics (2022).

48. H. F. Robey, L. Berzak Hopkins, J. L. Milovich and N. B. Meezan, Physics of Plasmas **25** (1) (2018).

49. A. L. Kritcher, D. T. Casey, C. A. Thomas, A. B. Zylstra, M. Hohenberger, K. Baker, S. Le Pape, B. Bachmann, S. Bhandarkar, J. Biener, T. Braun, D. Clark, L. Divol, T. Döppner, D. Hinkel, C. Kong, D. Mariscal, M. Millot, J. Milovich, A. Nikroo, A. Pak, N. Rice, H. Robey, M. Stadermann, J. Sevier, D. Strozzi, C. Weber, C. Wild, B. Woodworth, J. Edwards, D. A. Callahan and O. A. Hurricane, Physics of Plasmas **27** (5) (2020).

50. M. Hohenberger, D. T. Casey, A. L. Kritcher, A. Pak, A. B. Zylstra, C. A. Thomas, K. L. Baker, S. Le Pape, B. Bachmann, R. L. Berger, J. Biener, D. S. Clark, L. Divol, T. Döppner, V. Geppert-Kleinrath, D. Hinkel, H. Huang, C. Kong, O. L. Landen, J. Milovich, A. Nikroo, N. Rice, H. Robey, M. Schoff, J. Sevier, K. Sequoia, M. Stadermann, D. Strozzi, P. L. Volegov, C. Weber, C. Wild, B. Woodworth, D. A. Callahan and O. A. Hurricane, Physics of Plasmas **27** (11) (2020).

51. A. B. Zylstra, A. L. Kritcher, O. A. Hurricane, D. A. Callahan, K. Baker, T. Braun, D. T. Casey, D. Clark, K. Clark, T. Doppner, L. Divol, D. E. Hinkel, M. Hohenberger, C. Kong, O. L. Landen, A. Nikroo, A. Pak, P. Patel, J. E. Ralph, N. Rice, R. Tommasini, M. Schoff, M. Stadermann, D. Strozzi, C. Weber, C. Young, C. Wild, R. P. J. Town and M. J. Edwards, PHYSICAL REVIEW LETTERS **126** (2021).

52. A. L. Kritcher, A. B. Zylstra, D. A. Callahan, O. A. Hurricane, C. Weber, J. Ralph, D. T. Casey, A. Pak, K. Baker, B. Bachmann, S. Bhandarkar, J. Biener, R. Bionta, T. Braun, M. Bruhn, C. Choate, D. Clark, J. M. Di Nicola, L. Divol, T. Doeppner, V. Geppert-Kleinrath, S. Haan, J.

Heebner, V. Hernandez, D. Hinkel, M. Hohenberger, H. Huang, C. Kong, S. Le Pape, D. Mariscal, E. Marley, L. Masse, K. D. Meaney, M. Millot, A. Moore, K. Newman, A. Nikroo, P. Patel, L. Pelz, N. Rice, H. Robey, J. S. Ross, M. Rubery, J. Salmonson, D. Schlossberg, S. Sepke, K. Sequoia, M. Stadermann, D. Strozzi, R. Tommasini, P. Volegov, C. Wild, S. Yang, C. Young, M. J. Edwards, O. Landen, R. Town and M. Herrmann, Physics of Plasmas **28** (7) (2021).

53. A. B. Zylstra, A. L. Kritcher, O. A. Hurricane, D. A. Callahan, J. E. Ralph, D. T. Casey, A. Pak, O. L. Landen, B. Bachmann, K. L. Baker, L. Berzak Hopkins, S. D. Bhandarkar, J. Biener, R. M. Bionta, N. W. Birge, T. Braun, T. M. Briggs, P. M. Celliers, H. Chen, C. Choate, D. S. Clark, L. Divol, T. Döppner, D. Fittinghoff, M. J. Edwards, M. Gatu Johnson, N. Gharibyan, S. Haan, K. D. Hahn, E. Hartouni, D. E. Hinkel, D. D. Ho, M. Hohenberger, J. P. Holder, H. Huang, N. Izumi, J. Jeet, O. Jones, S. M. Kerr, S. F. Khan, H. Geppert Kleinrath, V. Geppert Kleinrath, C. Kong, K. M. Lamb, S. Le Pape, N. C. Lemos, J. D. Lindl, B. J. MacGowan, A. J. Mackinnon, A. G. MacPhee, E. V. Marley, K. Meaney, M. Millot, A. S. Moore, K. Newman, J. M. G. Di Nicola, A. Nikroo, R. Nora, P. K. Patel, N. G. Rice, M. S. Rubery, J. Sater, D. J. Schlossberg, S. M. Sepke, K. Sequoia, S. J. Shin, M. Stadermann, S. Stoupin, D. J. Strozzi, C. A. Thomas, R. Tommasini, C. Trosseille, E. R. Tubman, P. L. Volegov, C. R. Weber, C. Wild, D. T. Woods, S. T. Yang and C. V. Young, Physical Review E **106** (2) (2022).

54. A. L. Kritcher, A. B. Zylstra, D. A. Callahan, O. A. Hurricane, C. R. Weber, D. S. Clark, C. V. Young, J. E. Ralph, D. T. Casey, A. Pak, O. L. Landen, B. Bachmann, K. L. Baker, L. Berzak Hopkins, S. D. Bhandarkar, J. Biener, R. M. Bionta, N. W. Birge, T. Braun, T. M. Briggs, P. M. Celliers, H. Chen, C. Choate, L. Divol, T. Döppner, D. Fittinghoff, M. J. Edwards, M. Gatu Johnson, N. Gharibyan, S. Haan, K. D. Hahn, E. Hartouni, D. E. Hinkel, D. D. Ho, M. Hohenberger, J. P. Holder, H. Huang, N. Izumi, J. Jeet, O. Jones, S. M. Kerr, S. F. Khan, H.

Geppert Kleinrath, V. Geppert Kleinrath, C. Kong, K. M. Lamb, S. Le Pape, N. C. Lemos, J. D. Lindl, B. J. MacGowan, A. J. Mackinnon, A. G. MacPhee, E. V. Marley, K. Meaney, M. Millot, A. S. Moore, K. Newman, J. M. G. Di Nicola, A. Nikroo, R. Nora, P. K. Patel, N. G. Rice, M. S. Rubery, J. Sater, D. J. Schlossberg, S. M. Sepke, K. Sequoia, S. J. Shin, M. Stadermann, S. Stoupin, D. J. Strozzi, C. A. Thomas, R. Tommasini, C. Trosseille, E. R. Tubman, P. L. Volegov, C. Wild, D. T. Woods and S. T. Yang, Physical Review E **106** (2), 025201 (2022).

55. O. L. Landen, J. D. Lindl, S. W. Haan, D. T. Casey, P. M. Celliers, D. N. Fittinghoff, N. Gharibyan, V. N. Goncharov, G. P. Grim, E. P. Hartouni, O. A. Hurricane, B. J. MacGowan, S. A. MacLaren, K. D. Meaney, M. Millot, J. L. Milovich, P. K. Patel, H. S. Robey, P. T. Springer, P. L. Volegov and M. J. Edwards, Physics of Plasmas **28** (4) (2021).

56. R. Tommasini, D. T. Casey, D. Clark, A. Do, K. L. Baker, O. L. Landen, V. A. Smalyuk, C. Weber, B. Bachmann, E. Hartouni, E. V. Marley, M. Millot, J. Milovich, R. C. Nora, A. E. Pak, D. Schlossberg, B. Woodworth, T. M. Briggs, D. M. Holunga, A. Nikroo and M. Stadermann, Phys. Rev. Lett. (2023).

57. J. D. Lindl, S. W. Haan and O. L. Landen, Physics of Plasmas **30**, 012705 (2023).

58. J. D. Lindl, S. W. Haan, O. L. Landen, A. R. Christopherson and R. Betti, Physics of Plasmas **25** (12), 122704 (2018).

59. B. Cheng, T. J. T. Kwan, S. A. Yi, O. L. Landen, Y. M. Wang, C. J. Cerjan, S. H. Batha and F. J. Wysocki, Phys Rev E **98** (2-1), 023203 (2018).

FIGURE CAPTIONS

Figure 1 Drawing of the frustraum used on the NIF. It consists of two conical frustum-shaped hohlraums joined together along the equator of the capsule.

Figure 2 Effect of a change in delta lambda, 0 Å(N200108) to 0.5 Å(N211017), between the inner and outer cones on the P2 mode of the hotspot shape from neutron imaging.

Figure 3 Effect of an outer beam pointing change, on the P2 mode of the hotspot shape from neutron imaging. a) shows a change in where the 50 degree beams hit the wall as the pointing is changed. b) Plot of the P2 from a 0.1 mm pointing change in the outer 44.5 and 50 deg. cones between the pair of shots, N200721 and N201018, and a 0.2 mm pointing change in the outer 44.5 and 50 deg. cones between the pair of shots, N200217 and N200108.

Figure 4 Effect of a frustraum wall angle change on the P2 mode of the hotspot shape from neutron imaging. a) Schematic showing the wall angle change from 23 deg.(N210608) to 25 deg.(N210724). b) Plot of the measured P2 vs. wall angle(blue) and P2 vs. wall angle(red) corrected for hotspot motion for a measured hotspot vector of 130 km/sec, θ=109, ϕ=239 for N210608 and 144 km/sec, θ=139, ϕ=266 for N210724.

Figure 5 Symmetry plot of the x-ray P2 shape in experiments conducted in the Frustraum platform through calendar year 2021. These experiments include three different capsule inner radii, 1050, 1200 and 1400 μm, three wall angles 21, 23 and 25 degrees and three frustraum equatorial diameters, 7, 9.26 and 9.75 mm. A correction of the P2 shape due to the hotspot motion for two of

the experiments is shown as the green circles with the red arrows showing the change in P2. The bubble size is proportional to the inner radius of the ablator capsule to the 5^{th} power.

Figure 6 a) Hotspot radius, M0, vs. the initial capsule radius showing similar compression ratios. b) Capsule mode M2/M0 perturbation caused by to two 800 μm square uncoated 2D-ConA windows at the equatorial hohlraum wall, at phi angles of 78.75 and 258.75 degrees, for different campaigns on the NIF as a function of the solid angle of the windows from the capsule.

Figure 7 Images of the x-ray hotspot shape as a function of time for the symmetry capsule experiment N201018 are shown in (a. The images show two bright ~horizontal lines converging toward the axis along with a bright feature injected into the hotspot from the fill tube. The mass attributed to the line features is estimated using both a snow plow model (b and a drag model (c.

Figure 8 a) Laser pulse shapes used for the two layered implosions, N210117(black) and N210725(red). The second layered implosion, N210725, used more energy and reduced the peak power, both of which reduced the coast time of the implosion. The flux, measured by the Dante diagnostic, for N210117(green) along with the analytic(blue) time dependent flux valid once the laser is turned off. b) Peak implosion velocity(red) and coast time(blue) as a function of the radiation temperature at peak velocity, determined from a Rocket model of N210117 with increasing laser energy.

Figure 9 Reconstructed 3-D neutron hotspot shapes for the two layered implosions conducted in the frustraum. To the upper left is displayed the fluence compensated images.Figure 10 a) Bubble plot of DSR vs. coast time for all of the HDC campaigns conducted on the NIF with no corrections to the data. The bubble size depends on the tungsten areal density present in each of the capsules used in the implosions. b) the DSR is corrected for mode 1, mode 2 and yield amplification.

Figure 10 a) Down-scattered ratio divided by the initial ice thickness as a function of coast time. B) Down-scattered ratio divided by the initial ice thickness as a function of coast time corrected for yield amplification, mode 1 and mode 2.

Figure 11 Bubble plot of capsule absorbed energy vs. coast time for all of the HDC campaigns conducted on the NIF. The bubble size depends on the yield amplification for each of the implosions.

Figure 12 Bubble plot of primary neutron yield vs. coast time for all of the HDC campaigns conducted on the NIF. The bubble size depends on the radius of the capsule to the fifth power for each of the implosions.

Figure 13 Generalized Lawson criterion using the $GLC(ITFXmod) = 0.27(ITFXmod)^{0.6}$ plotted against the $GLC(P_{stag}, E_{hs}) = (P_{stag}/420)(E_{hs}/30)^{0.5}$ is shown in Fig. 14a. Generalized Lawson criterion using the $GLC(DSR, Tion) = 0.187(DSR)^{1.55}(T_{ion})^{3.5}$ plotted against the $GLC(P_{stag}, E_{hs}) = (P_{stag}/420)(E_{hs}/30)^{0.5}$ is shown in Fig. 14b.

Figure 14 Bubble plot of the ion temperature vs. coast time for all of the HDC campaigns conducted on the NIF. The dashed line represents the minimum ion temperature vs. coast time required for ignition using the GLC defined in Fig. 14b along with the DSR represented by the dashed line in Fig. 11. The bubble size depends on the radius of the capsule to the fifth power for each of the implosions. All experiments with coast time less than 1 ns have DSRs lower than the dashed line in Fig. 11 and hence would require a higher T_{ion} for ignition than the minimum T_{ion} line.

Figure 15 Plot of the simulated DSR degradation, black cirecles, due to mode 2 shape. The dashed red line denotes an analytic fit of $V^{2/3}/S$ to the DSR as a function of P2/P0 where V is the volume

of a spheroid, S is the surface area of the spheroid, P2 is the mode 2 of the fuel and P0 is the fuel radius.

Table 1 Summary of target and drive characteristics along with experimentally measured and inferred performance parameters for the frustraum shots and the best performing BigFoot, HDC and HyE1100 layered implosions.

FIGURES

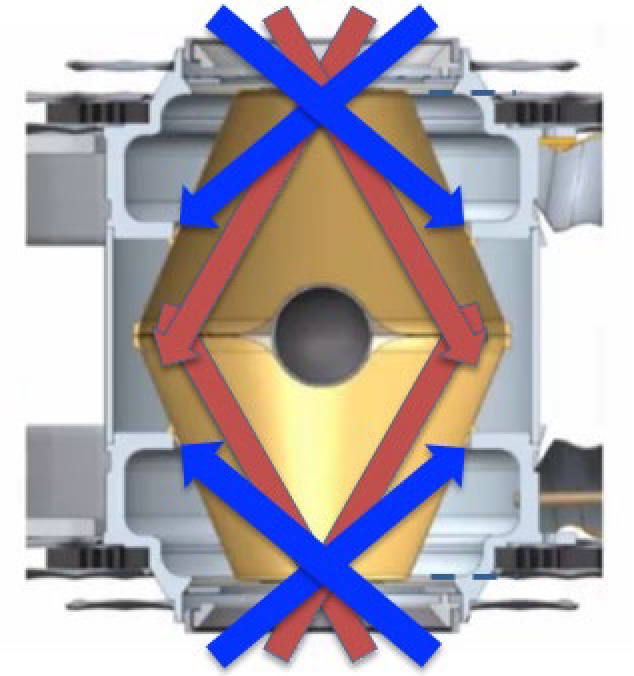

Figure 1

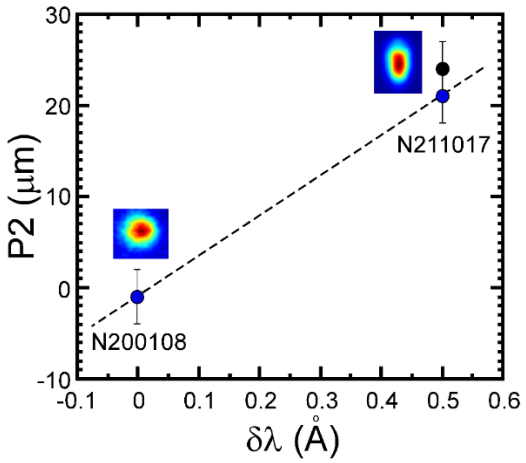

Figure 2

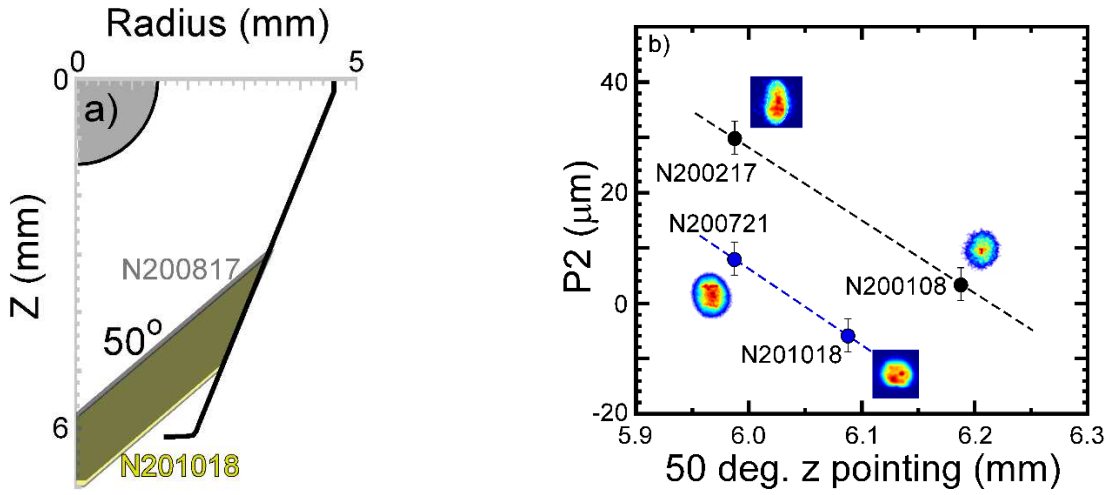
Radius (mm)
0
5
a)
Z (mm)
N200817
50°
6
N201018
b)
40
20
0
-20
P2 (μm)
N200217
N200721
N200108
N201018
5.9
6.0
6.1
6.2
6.3
50 deg. z pointing (mm)

Figure 3

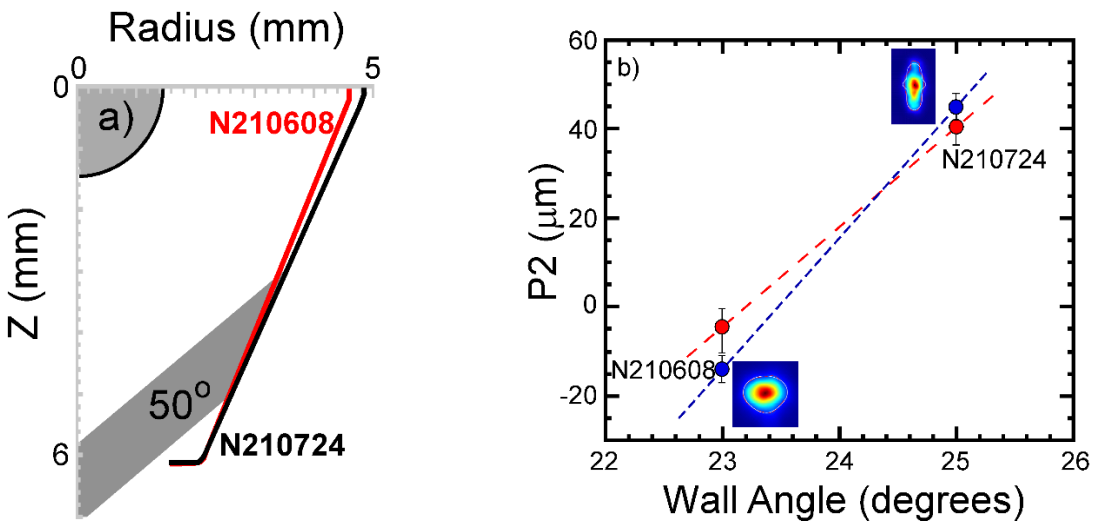
Radius (mm)
0
5
a)
N210608
Z (mm)
50°
6
N210724
b)
60
40
20
0
-20
P2 (μm)
N210724
N210608
22
23
24
25
26
Wall Angle (degrees)

Figure 4

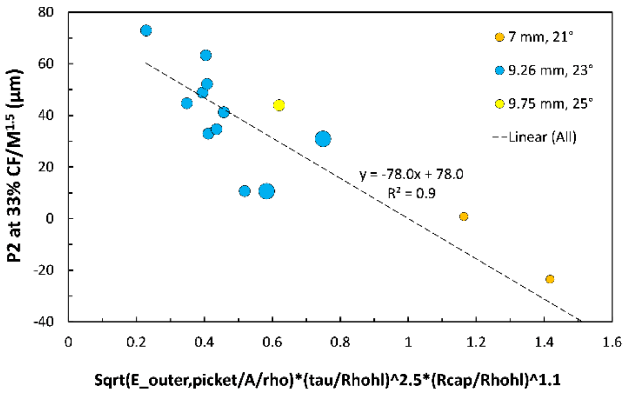
P2 at 33% CF/M^1.5 (µm)
Sqrt(E_outer,picket/A/rho)*(tau/Rhohl)^2.5*(Rcap/Rhohl)^1.1
7 mm, 21°
9.26 mm, 23°
9.75 mm, 25°
Linear (All)
y = -78.0x + 78.0
R² = 0.9
80
60
40
20
0
-20
-40
0
0.2
0.4
0.6
0.8
1
1.2
1.4
1.6

Figure 5

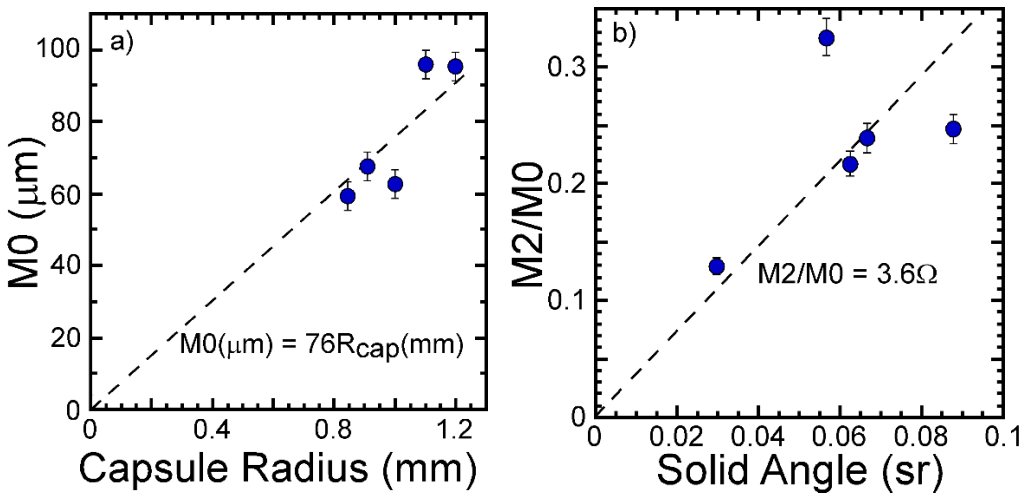
a)
M0 (μm)
Capsule Radius (mm)
M0(μm) = 76R_cap(mm)
b)
M2/M0
Solid Angle (sr)
M2/M0 = 3.6Ω

Figure 6

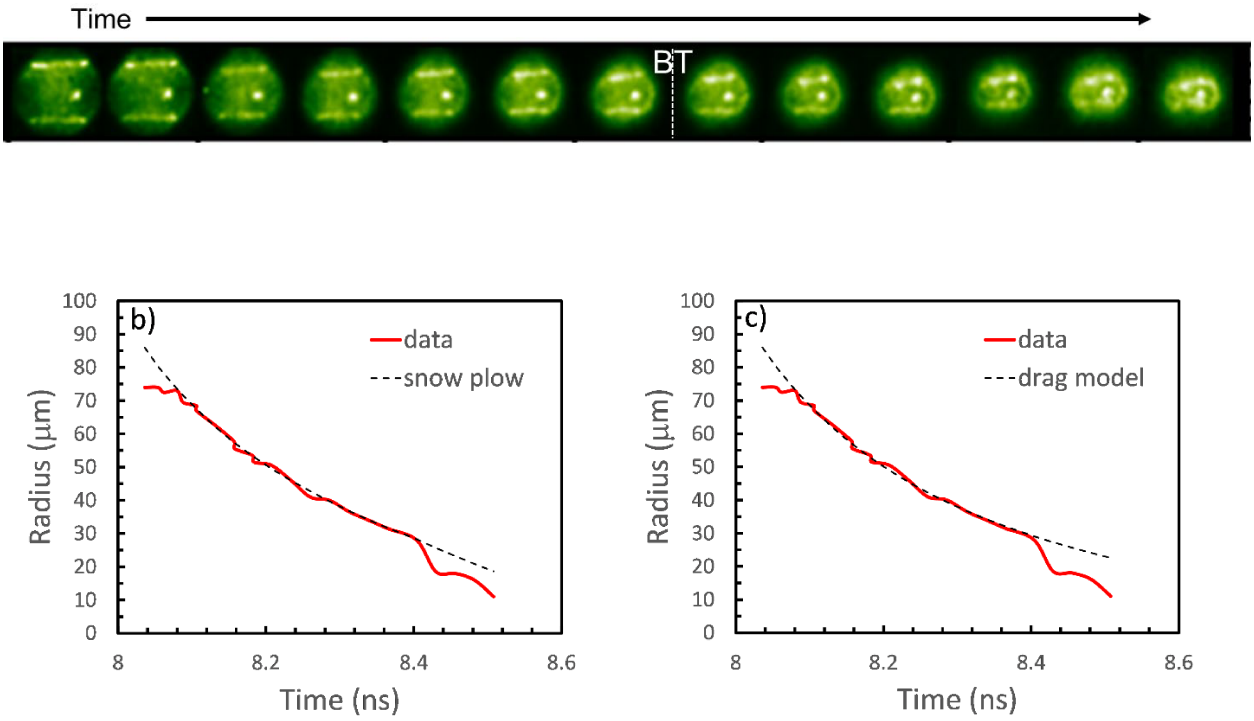
Time
BT
b)
data
snow plow
Radius (μm)
Time (ns)
c)
data
drag model
Radius (μm)
Time (ns)

Figure 7

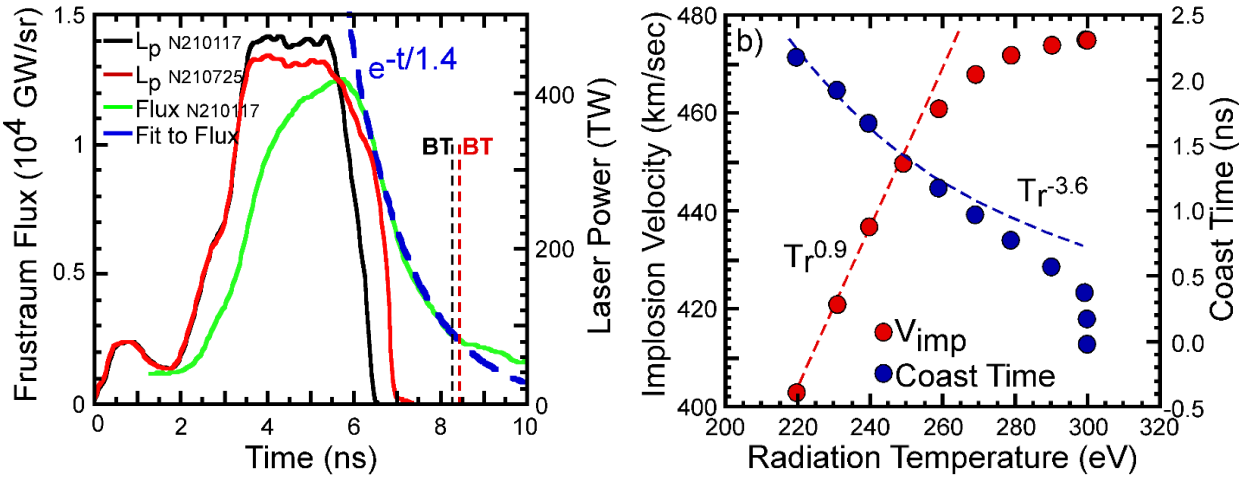
Frustraum Flux (10^4 GW/sr)
Laser Power (TW)
Time (ns)
Lp N210117
Lp N210725
Flux N210117
Fit to Flux
e-t/1.4
BT
BT
b)
Implosion Velocity (km/sec)
Coast Time (ns)
Radiation Temperature (eV)
Tr^0.9
Tr^-3.6
Vimp
Coast Time

Figure 8

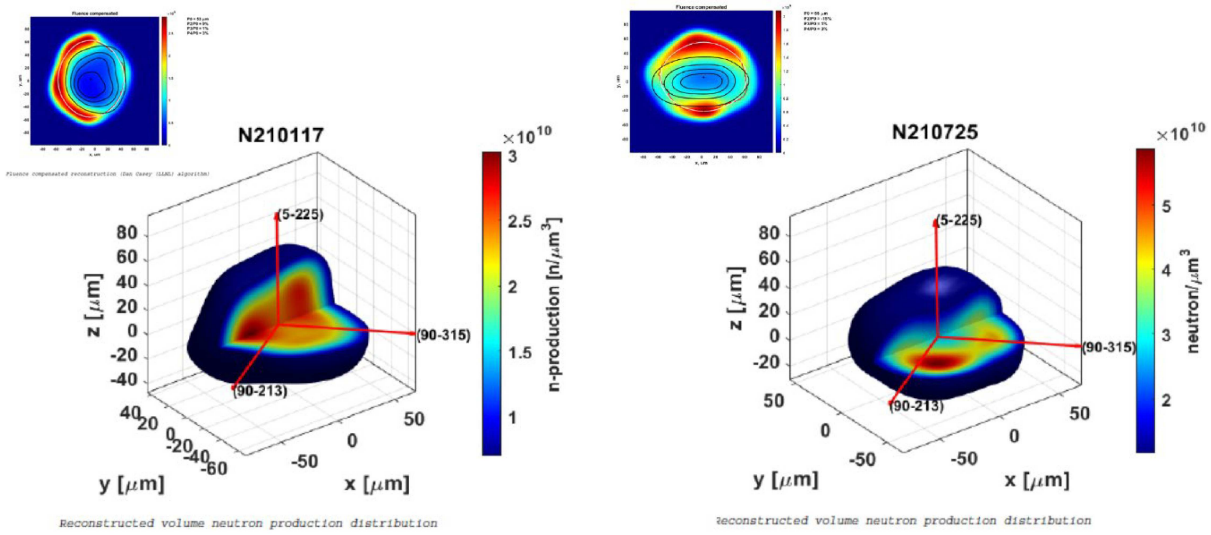
N210117
×10^10
3
2.5
2
1.5
1
n-production [n/μm^3]
(5-225)
(90-315)
(90-213)
z [μm]
y [μm]
x [μm]
Reconstructed volume neutron production distribution
N210725
×10^10
5
4
3
2
neutron/μm^3
(5-225)
(90-315)
(90-213)
z [μm]
y [μm]
x [μm]
Reconstructed volume neutron production distribution

Figure 9

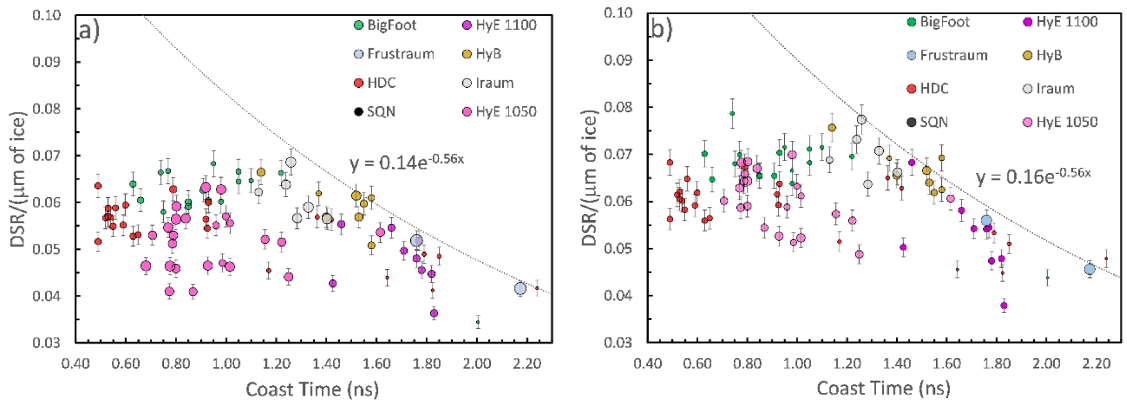
a)
BigFoot
HyE 1100
Frustraum
HyB
HDC
Iraum
SQN
HyE 1050
y = 0.14e-0.56x
DSR/(µm of ice)
Coast Time (ns)
b)
y = 0.16e-0.56x

Figure 10

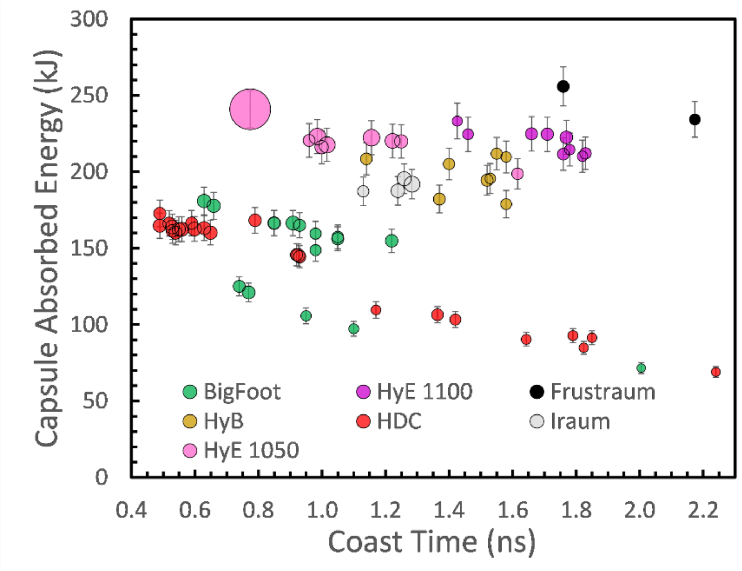
Capsule Absorbed Energy (kJ)
300
250
200
150
100
50
0
0.4
0.6
0.8
1.0
1.2
1.4
1.6
1.8
2.0
2.2
Coast Time (ns)
BigFoot
HyB
HyE 1050
HyE 1100
HDC
Frustraum
Iraum

Figure 11

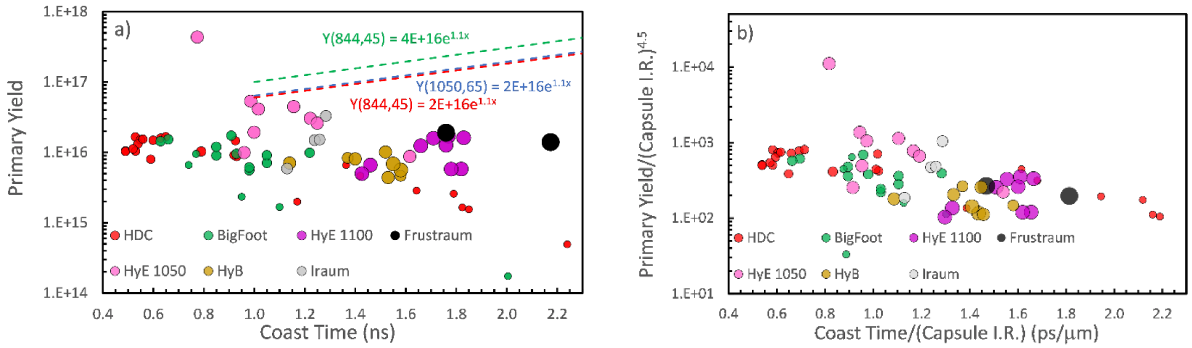
a)
Y(844,45) = 4E+16e^1.1x
Y(1050,65) = 2E+16e^1.1x
Y(844,45) = 2E+16e^1.1x
Primary Yield
Coast Time (ns)
HDC
BigFoot
HyE 1100
Frustraum
HyE 1050
HyB
Iraum
b)
Primary Yield/(Capsule I.R.)^4.5
Coast Time/(Capsule I.R.) (ps/μm)

Figure 12

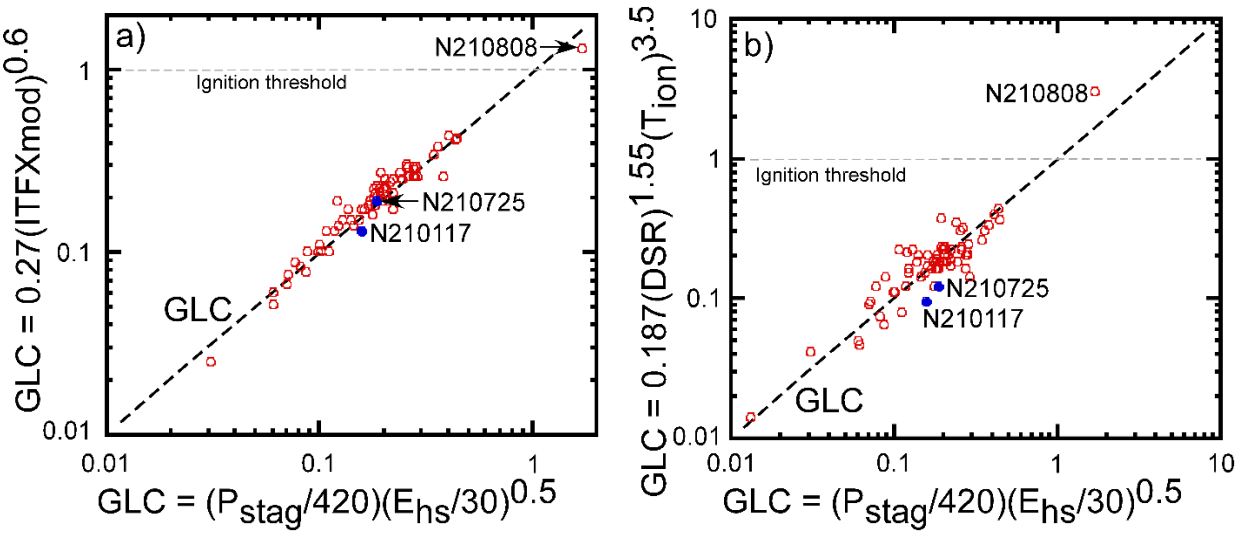
a)
N210808
Ignition threshold
N210725
N210117
GLC
GLC = 0.27(ITFXmod)^0.6
GLC = (Pstag/420)(Ehs/30)^0.5
b)
N210808
Ignition threshold
N210725
N210117
GLC
GLC = 0.187(DSR)^1.55(Tion)^3.5
GLC = (Pstag/420)(Ehs/30)^0.5

Figure 13

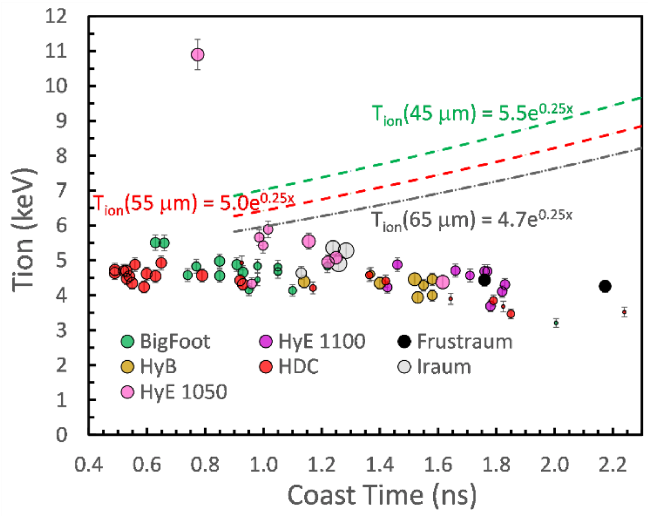
Tion (keV)
Coast Time (ns)
T_{ion}(45 μm) = 5.5e$^{0.25x}$
T_{ion}(55 μm) = 5.0e$^{0.25x}$
T_{ion}(65 μm) = 4.7e$^{0.25x}$
BigFoot
HyB
HyE 1050
HyE 1100
HDC
Frustraum
Iraum

Figure 14

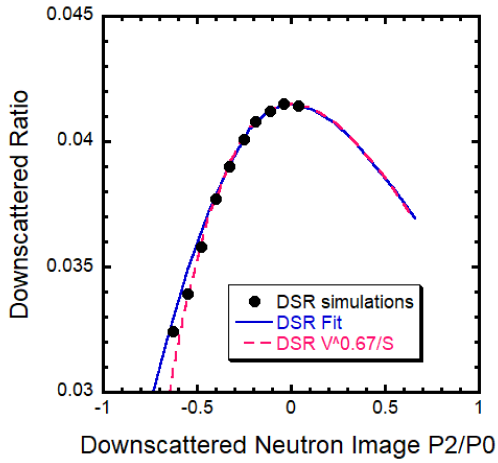
0.045
0.04
0.035
0.03
Downscattered Ratio
-1
-0.5
0
0.5
1
Downscattered Neutron Image P2/P0
DSR simulations
DSR Fit
DSR V^0.67/S

Figure 15

	Frustraum N210117	Frustraum N210725	HyE1100 N191110	BigFoot N180128	HDC N170827
HDC capsule I.R. (μm)	1200	1200	1100	950	910
W dopant areal density (%μm)	7	7	5.4	6	6.6
Ice layer thickness (μm)	58.6	50	65.5	49.4	55
Laser Energy (MJ)	1.6	1.7	1.9	1.8	1.8
Coast Time (ns)	2.17	1.76	1.77	0.91	0.53
Neutron Image, P0 (μm)	44.9	46	41.9	31	28.4
Neutron Image, P2 (μm)	4.5	-20.7	-4.4	0.6	-7.7
Burn width (ps)	209	197	166	152	154
Ion Temperature T_{ion}(DT) (keV)	4.26	4.44	4.69	4.88	4.7
Downscattered Ratio DSR (%)	2.44	2.59	3.4	3.09	3.14
DSR/(initial ice thickness) (%/μm)	0.042	0.052	0.052	0.063	0.058
DT neutron yield (13-15 MeV) ($x10^{16}$)	1.4	1.9	1.71	1.73	1.66
Yield Amplification	1.8	2.2	2.4	2.9	2.9
Capsule absorbed energy E_{cap} (kJ)	234	256	223	166	164
Hotspot Energy E_{hs} (kJ)	7.6	9.6	7.8	5	4.5
Hotspot Pressure P_{hs} (Gbar)	132	140	168	271	301
GLC (P_{hs} /420)sqrt(E_{hs} /30)	0.16	0.19	0.2	0.26	0.28

Table 1